Agricultural and Forest Meteorology 383 (2026) 111129

Contents lists available at ScienceDirect

Agricultural and Forest Meteorology

journal homepage: www.elsevier.com/locate/agrformet

Dynamic stability and canopy structure drive spatio-temporal variability of greenhouse gas concentrations in the sub-canopy of a temperate spruce forest

Mohammad Abdoli [a,d,*], Karl Lapo [b], Christoph K. Thomas [a,c]

[a] Micrometeorology Group, University of Bayreuth, Bayreuth, Germany
[b] Until Fall 2021: Micrometeorology Group, University of Bayreuth, Bayreuth, Germany
[c] Bayreuth Center for Ecology and Environmental Research (Bayceer), University of Bayreuth, Bayreuth, Germany
[d] Physical Geography and Climatology, Institute of Geography, RWTH Aachen University, Aachen, Germany

ARTICLE INFO

Keywords:
Greenhouse gases
Random forest
Wind regimes
Thermal stratification
Canopy flows
Eddy covariance

ABSTRACT

We investigated the micrometeorological controls on spatio-temporal variability of CO_2, CH_4, and H_2O mixing ratios in the horizontal and vertical dimensions within a temperate forest canopy using high-resolution measurements from sensor networks and machine learning techniques. The main objective was to identify the governing factors controlling scalar gas variability within the sub-canopy and to assess how static stability and thermal stratification influence scalar mixing processes under varying wind regimes. Scalar variability was characterized in both the vertical and horizontal across weak- and strong-wind regimes, defined using sub- and above-canopy turbulence statistics. A Random Forest model was employed to identify key drivers of scalar variability showing that in the sub-canopy it is primarily controlled by shear-induced turbulence during strong winds and by buoyancy during weak winds. Under strong wind conditions, CO_2 variability is mainly influenced by TKE and dynamic stability, whereas air temperature becomes the key driver under weak-wind conditions. For CH_4, temperature remains an important factor across all conditions, with wind shear playing a role during strong winds and horizontal advection influencing its variability under weak winds. H_2O variability is closely tied to temperature in all wind regimes, reflecting evapotranspiration dynamics and energy distribution. Additionally, vertical profiles of potential temperature from Fiber-Optic Distributed Sensing (FODS) were clustered using k-means to classify stratification regimes, showing that unstable temperature profiles promote mixing and reduce variability, whereas stable stratification suppresses mixing and enhances scalar variability. Horizontal and vertical CO_2 and CH_4 spatial variability could be explained by thermal stratification and horizontal wind, integrating effects of turbulence and radiation, while H_2O variability was primarily governed by evapotranspiration dynamics and energy availability, particularly during early morning and late afternoon transition periods. The diurnal course of carbon dioxide flux across the forest revealed a pronounced contrast between above-canopy and sub-canopy with regime-dependent differences in vertical coupling and "flushing" events that enhance subcanopy CO_2 transport under weakly turbulent conditions. Our results emphasize the critical role of the non-linear interplay of turbulence, static stability, canopy structure, and enthalpie inputs in shaping fine-scale greenhouse gas mixing and transport. They also demonstrate the effectiveness of dense sensor networks combined with machine learning methods to enhance process-level understanding of gas exchange dynamics within forest sub-canopies.

1. Introduction

Forests play a substantial role in land-atmosphere interaction as they uptake carbon dioxide through photosynthesis. Covering approximately 30 % of the Earth's surface, forests account for roughly 45 % of terrestrial carbon storage and contribute to 50 % of net primary production (Bonan, 2008). The intricate nature of forest's spatial variability makes it challenging to understand transport and mixing processes within their

* Corresponding author.
E-mail address: Mohammad.abdoli@geo.rwth-aachen.de (M. Abdoli).

https://doi.org/10.1016/j.agrformet.2026.111129
Received 19 October 2025; Received in revised form 26 February 2026; Accepted 10 March 2026
Available online 20 March 2026

canopies and sub-canopy regions. Various factors including diverse canopy structures, clearings, and geometric configurations can significantly impact turbulence patterns and scalar variability and subsequently affect the exchange and budgets of mass, momentum, and heat within the canopy (Dupont et al., 2012; Thomas, 2011). While numerous studies have examined the carbon dioxide (CO_2) budget and transport within sub-canopy environments, there remains a noticeable scarcity of research investigating the spatiotemporal variations in the most important greenhouse scalar fields of carbon dioxide (CO_2), methane (CH_4), and water vapor (H_2O) in the sub-canopy of temperate forests for different wind regimes which are foundational for comprehensively analyzing transport processes, and mixing dynamics in the forest. Wind regimes can be stratified into strong- or weak-wind conditions. Strong wind conditions occur when the wind speed exceeds a certain threshold, above which shear-driven turbulence rapidly increases with increasing the bulk shear. In contrast, weak wind conditions correspond to wind speeds below this threshold, where turbulence is not driven by bulk shear but rather generated locally through non-stationary and likely non-turbulent motions (Liang et al., 2014; Mahrt et al., 2015; Sun et al., 2012). Learning more about the variability of scalars gains special attention due to the persistence of weak-wind situations in sub-canopy during day- and nighttime when the air near the ground reaches close to neutral or slightly stable stratification and causes conventional theories of turbulence, including the Monin-Obukhov similarity theory, the Kolmogorov spectrum, and Taylor's hypothesis of frozen turbulence to collapse (Belcher et al., 2008).

Various research efforts have explored the variability of sub-canopy scalar gas mixing ratios, as well as temperature and wind, using observational measurement networks in the forest. Wilson and Meyers (2001) assessed the variability of sub-canopy using three Eddy Covariance (EC) systems that were separated vertically and horizontally. Their primary focus was to examine the representativeness of a single EC system in estimating soil respiration by examining the variation in turbulent fluxes of carbon dioxide, latent heat, and sensible heat. They concluded that the variability is time-dependent: as the temporal averaging period increases, the spatial variability of these fluxes decreases. Feigenwinter et al. (2010) investigated anomalous CO_2 patterns in Norunda, Sweden, during the late summer. Elevated CO_2 mixing ratios, peaking at 500 μmol mol^{-1} below 30 m above ground level (agl), exhibited substantial vertical and horizontal gradients, resulting in variable advective fluxes. This build-up of CO_2 occurred as canopy stratification shifted from stable to neutral conditions during the second part of the night, moving largest temperature and CO_2 gradients from near the ground to the forest crown space. Thomas (2011) investigated the space-time structure of wind and temperature fields within a dense forest sub-canopy in moderately complex terrains. Using a network of ten sensor stations and advanced stochastic techniques, he revealed significant differences in the space-time characteristics of wind and temperature fields, with short-lived, small-scale motions dominating wind variability and diurnal temperature oscillations driving temperature signal variability over larger time scales. Nevertheless, this study did not incorporate scalar gas mixing ratios to assess their interrelated variability within the sub-canopy system. Additionally, Oliveira et al. (2018) examined night-time wind and scalar variability within and above an Amazonian canopy by assessing nocturnal turbulent kinetic energy (TKE) and the exchange of energy, CO_2, and ozone (O_3) between the Amazon forest and the atmosphere. Spectral analysis revealed that a substantial portion of the variability observed during intermittent nights can be attributed to low-frequency, non-turbulent fluctuations. Additionally, intermittent turbulence can lead to substantial fluxes impacting CO_2 and O_3 mixing ratios, highlighting the complex interplay of stability and turbulence in nocturnal atmospheric conditions. This study focuses exclusively on mixing ratio profiles and flow statistics in the vertical and horizontal directions. Given the inherent horizontal variability of canopy structure, soil properties, and ground surface conditions, these aspects are essential for a comprehensive characterization of transport and mixing processes within the canopy. Despite various studies investigating the variability of greenhouse gases, wind, and temperature in the sub-canopy, there is a lack of comprehensive research on the spatio-temporal variability of CO_2, H_2O, and CH_4 mixing ratios. Moreover, there is a need to identify the driving forces of each gas while highlighting the differences across different wind regimes.

Besides experimental observations, the Large-Eddy Simulation (LES) and other modeling techniques have been extensively utilized to investigate flow and mixing ratio variability in forest environments (Kanani-Sühring and Raasch, 2015). However, simulations using advanced models are computationally intensive and often display significant biases compared to observational data (Girach et al., 2022). In contrast, machine learning (ML) models, which leverage observational datasets, are expected to generate outputs with lower biases due to their data-driven nature and have considerably shorter runtimes than conventional models. This has led to a growing recognition of the potential benefits of artificial intelligence (AI) and ML in atmospheric sciences (Arcomano et al., 2020). We employed ML approach to determine scalar gas driving forces in forest canopies for the purpose of: (i) identifying the most critical variables for modelling scalar gas variability and (ii) clustering vertical temperature profiles to evaluate scalar gas variability under different vertical temperature stratifications.

Our methodology relies on an extensive and unique observational dataset from Fiber-Optic Distributed Sensing (FODS) for continuous temperature observation in combination with a scalar gas sampling network for measuring CO_2, CH_4, and H_2O mixing ratios in both vertical and horizontal orientations, and the deployment of four EC systems. These advanced tools and data sources enable us to achieve our two key research objectives: (i) To elucidate the governing factors underlying the scalar gas variability observed within the sub-canopy, encompassing the dynamic fields of CO_2, H_2O, and CH_4. (ii) To understand the influence of static stability and thermal stratification on scalar mixing processes in the sub-canopy environment under different wind flow regimes. The integration of these innovative observational methods and analytical techniques empowers us to address these fundamental research inquiries comprehensively and advance our understanding of complex environmental dynamics within forested ecosystems.

2. Materials and methods

2.1. Study site

The Large-eddy ObsErvatory Waldstein Experiment 2020 (LOEWE20) was conducted at the long-term ecosystem flux site Waldstein-Weidenbrunnen (DE-Bay) between August and November 2020. The Waldstein is a forested site in the Fichtelgebirge mountains in the Lehstenbach catchment. The forest is dominated by Norway spruce (Picea abies) and is characterized by variable tree heights and densities. The canopy height was measured to be 27 m in 2011 (Serafimovich et al., 2011). The sub-canopy vegetation is moderately dense with a cumulative plant area index of 0.7 m^2m^{-2}, characterized by shrubs $\leq$1 m in height. The plant area index (PAI) is 5.6 $\pm$ 2.1 m^2m^{-2} for the overstory trees and 3.5 m^2m^{-2} for the understory trees. At the Waldstein site, the above-canopy flow is dominated by westerly and southeasterly winds with a wind speed range of 2 to 5 ms^{-1}; the understory flow is dominated by northerly and southwesterly winds with a range of 1 to 2 ms^{-1} (Foken, 2017).

The experimental configuration of LOEWE20 (Fig. 1) consisted EC systems together with fast-response high-resolution pressure transducers, Gas Sampling Network (GCSN), and FODS in a plot of approximately 200 m $\times$ 200 m extended in both vertical and horizontal directions.

2.2. Turbulent flux measurement

The LOEWE20 experiment includes four sensor packages. These

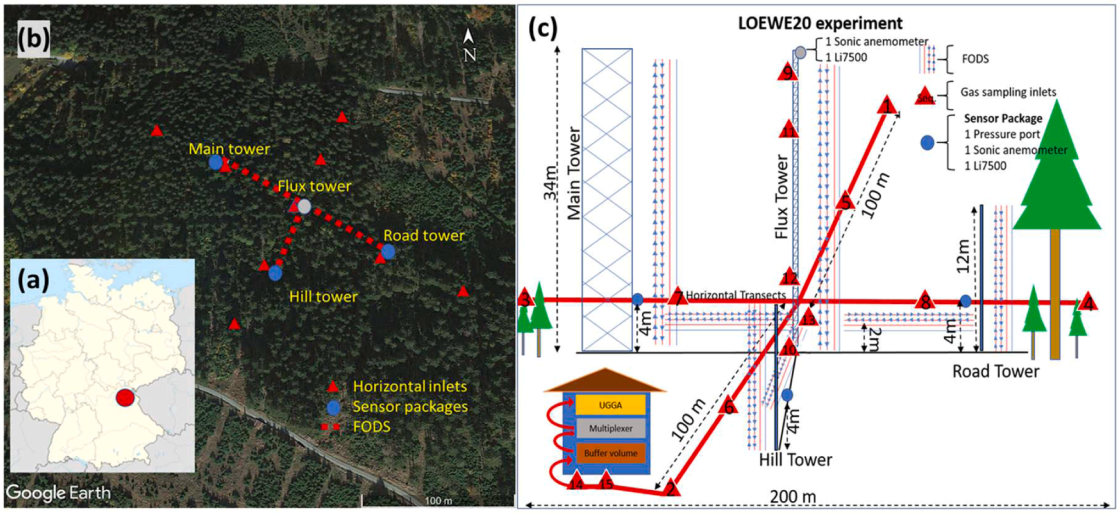

Fig. 1. (a) Location of the LOEWE20 experiment marked with a red dot on the map of Germany. (b) Layout of the measurement network showing the FODS arrays as dashed red lines, the horizontal inlets of the Gas Concentration Sampling Network (GCSN) as red triangles labelled S1–S8 and S12, and four vertical measurement towers with sensor packages indicated by blue solid points. (c) Detailed schematic of the experimental setup illustrating the vertical and horizontal FODS arrays, including two unconed fibers (one of which is heated) and two heated coned fibers, and the GCSN inlets in both vertical and horizontal configurations, along with the sensor packages placed at three positions at 4 m and one at 36 m height. UGGA refers to ultra-portable close-path greenhouse gas analyser.

sensors are positioned as follows: one at the top of the canopy at 36 m, and the remaining three at a height of 4 m agl. All of the sensor packages are equipped with a sonic anemometer (Model CSAT3, Campbell Scientific Inc., Logan, UT, USA), and an open-path infrared CO_2 / H_2O gas analyser (Licor 7500, LI-COR Biosciences, USA). Except for the flux tower, which is a long-term EC system at the study site, the other three stations are additionally equipped with a quad disk static pressure transducer (Model 745–16B, Paroscientific, Inc.). The data of sensor packages at 4 m were sampled at 20 Hz, and at the top of the 36 m flux tower at 10 Hz. All of the EC systems in this study use the same data processing and flux computation routine described in Appendix A of Thomas et al. (2009). Perturbation and averaging timescales of 10 min were used to compute the turbulent fluxes. Appendix A (Fig. A1) shows the time period of the data used in this study and the availability of different variables. It includes 3196 ten-minute intervals of EC and Gas Concentration Sampling Network (GCSN) data, along with 1248 intervals of available FODS observations from 10 September to 5 October 2020.

2.3. Gas concentration sampling network (GCSN)

In addition to measuring CO_2 and H_2O turbulent fluxes and concentrations using four EC systems, an ultra-portable close-path greenhouse gas analyser (UGGA, Los Gatos Research Inc.) was used to measure the scalar gas mixing ratios of CH_4, CO_2, and H_2O sampled from different vertical and horizontal inlets. An external air pump was used to draw air from each measurement inlet into the bottom of a 5-liter bottle-shaped buffer volume. The inlet of each tube at the measurement point was connected to a 1 μm Gelman filter (ACRO 50 PTFE; Gelman, Ann Arbor, Michigan, USA). Additionally, a nylon funnel was installed at each air intake to minimize particle and rain water droplets entering the tubing and filter. Two further tubes are attached to the top of the buffer volume, one connecting to the UGGA multiplexer and the other connected to an air pump set to a flow rate for continuous ventilation of the buffer volume.

The gas sampling multiplexer connected between the buffer volumes and the gas analyser allowed for sequencing between all inlets shown with red triangles (Fig. 1) of which 13 out of 15 inlets were positioned as vertical and horizontal ambient air inlets in the subcanopy and canopy spaces, and the remaining two were connected to 381 and 455 ppm reference CO_2 gases for continuous reference and validation. The sequencing time for sampling the 13 ambient air inlets was 7 min. The two reference gas inlets were measured for 90 s each after 11 full sequences of 13 ambient air inlets giving a total cycle time through all 15 inlets of 80 min. Figure A2 shows the schematic diagram of the designed buffer system and multiplexer, with the technical details provided in the appendix.

In post-processing, the initial 15 s of each measured sequence were discarded to allow for flushing the tubing and analyser's cavity to prevent cross-contamination between subsequent air samples. The remaining data were averaged to 10 min to synchronize with the turbulent flux measurements. The spatial standard deviation of scalar gas mixing ratios computed using the equation: $\widehat{\sigma}_{\chi_{h,v}} = 1/n \sum_0^n (\chi_n - \widehat{\chi})$, where $\widehat{\sigma}_{\chi_{h,\ v}}$ stands for vertical and horizontal spatial standard deviation of scalar gas mixing ratio, n is the number of inlets used and χ is the mixing ratio in each inlet. Due to the existing systematic gradient in the vertical scalar gas mixing ratio profile, the hourly average profile is subtracted from the vertical inlets before computing the spatial standard deviation. The inlets S9, S10, S11, S12, and S13 used for vertical and S1, S2, S3, S4, S5, S6, S7, S8, and S12 used for horizontal standard deviation computation. The accuracy of the UGGA device was determined to be −1.39 ppm for the 381 ppm and −0.04 ppm for the 455 ppm CO_2 reference gases. A cross-comparison of CO_2 and H_2O mixing ratios measured by the GCSN and EC systems at four EC stations is presented in the scatter plots in Fig. A3.

Based on the buffer system calculations presented in the Figure A2, the effective integration time of the air sampled within the buffer volume corresponds to approximately 2.2 min physically averaged gas mixing ratios. To further evaluate the stationarity assumption, we analyzed the power spectra of CO_2 and H_2O mixing ratios using 1-minute averaged data. In the 10-minute timescale range, the spectra exhibit a relatively flat energy distribution resulting from the physical averaging in the buffer volumes, indicating no enhanced variability that would violate the stationarity assumption. Moreover, the EC spectra follow the expected −5/3 slope within the inertial subrange and show no increased variance at frequencies corresponding to the 10-minute sampling interval ($f \approx 0.0024$ Hz). This supports the assumption of quasi-stationary conditions during the sequential measurements. The corresponding spectra for CO_2 and H_2O mixing ratios above and below the canopy are provided in Appendix Fig. A4.

2.4. Fiber-Optic distributed sensing

Wind speed and wind direction can be derived from FODS by actively heating the fiber and relating the resulting convective heat loss to atmospheric flow conditions (Thomas and Selker, 2021).The cooling rate of the heated fiber scales with wind speed, analogous to hot-wire anemometry (Sayde et al., 2015; van Ramshorst et al., 2020). Directional sensitivity is achieved by imprinting conical microstructures on paired fibers, termed coned fiber, which induce differential convective heat loss depending on the alignment of the flow relative to the microstructures (Lapo et al., 2020). This microstructure approach has been validated in a field experiments for measuring horizontal and vertical wind direction and speed using FODS (Abdoli et al., 2023; Freundorfer et al., 2021a).

In this study, a quartet of fiber-optic (FO) arrays is utilized for measuring distributed temperature, wind speed, and wind direction in both vertical and horizontal transects, as illustrated in Fig. 1. The FO arrays consist of two pairs of parallel coned and unconed FO cables, with one of the unconed and both coned fibers being heated using the Heat Pulse Unit (HPU) system (Model Heat Pulse System, Silixa, London, UK) and subject to a constant electric current of 4 Wm^{-1} to the stainless-steel sheath of the fiber-optic cable. One of the cores of the FO cable contains four 50 μm multimode bend-insensitive cores (inner tube diameter = 1.06 mm, outer diameter = 1.32 mm; Model C-Tube, Solifos AG, Switzerland; resistance = 1.8Ω m^{-1}) was connected to the Distributed Temperature Sensing (DTS) device (Model 5 km ULTIMA, Silixa, London, UK) with a sampling resolution of 0.127 m and temporal resolution of 1 s. The cones of the coned FO cables are constructed from polyethylene with a diameter and height of 12 mm, spaced at 2 cm intervals along the FO cable (Freundorfer et al., 2021b). Two warm and cold solid-phase calibration baths with a constant temperature were positioned at the beginning and end of the FO arrays to serve as calibration references (Thomas et al., 2022).

DTS measurements were conducted in a double-ended configuration using two channels of each DTS device (Van de Giesen et al., 2012). The start and end of each fiber were linked to two different channels, recording the temperature of the fiber by alternating every 3 s between the two channels. Each channel was saved individually and combined into a single dataset with a time resolution of 6 s during the data post-processing. The post-processing was carried out using the pyfocs code developed by Lapo and Freundorfer (2020), which employs the matrix inversion method utilizing constant temperature sections wrapped around warm and cold solid-state reference baths (des Tombe et al., 2020). The distributed horizontal wind speed (U_{FODS}) was derived using

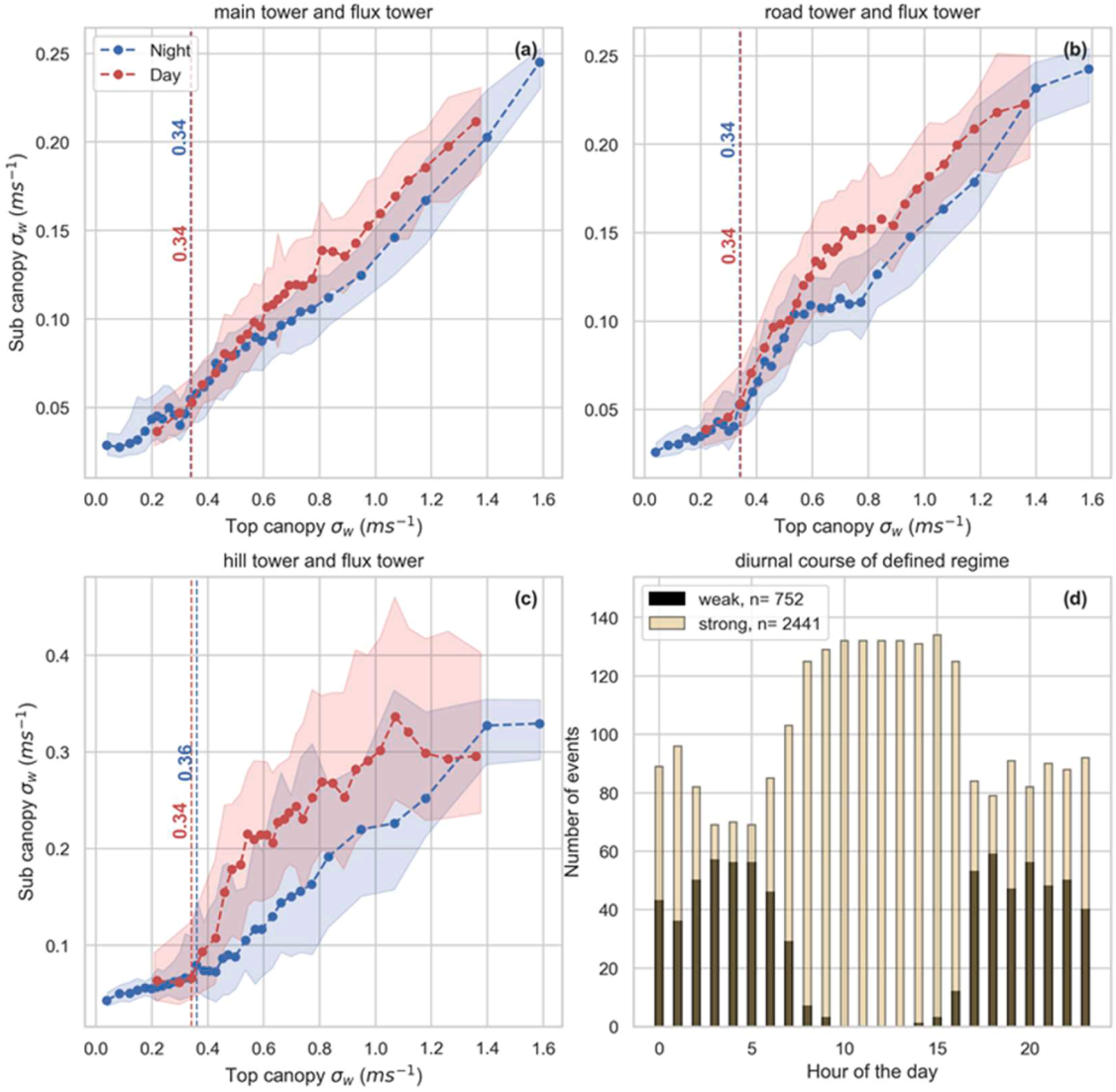

Fig. 2. Determining the thresholds of the weak-wind regime using σ_w in the sub-canopy and above-canopy for the main tower (a), road tower (b), and hill tower (c), along with the diurnal course of the defined regime for the entire sub-canopy. The shaded areas represent ±1 standard deviation from the mean.

paired heated and unheated FO cables in vertical FODS arrays, following the method described by van Ramshorst et al. (2020).

2.5. Defining wind regimes

We identified strong and weak wind regimes using the standard deviation of vertical wind velocity (σ_w) derived from three sub-canopy and one above-canopy EC systems. We postulate that a linear correlation between σ_w values above and below the canopy indicates sufficiently strong turbulence to maintain canopy coupling. Conversely, when above-canopy σ_w is insufficient to induce turbulence within the sub-canopy, decoupling occurs. Freundorfer et al. (2019) caution that the observed linear relationship under strong wind conditions may be confounded by the superposition of weak and strong wind regimes. Nevertheless, we opted to use σ_w as the primary indicator rather than friction velocity (u_*), as σ_w has been recognized in the literature as a suitable metric for diagnosing canopy decoupling in forests (Acevedo et al., 2009; Thomas et al., 2013) and has been shown to yield similar thresholds to those based on u_* (Stiegler et al., 2023).

To define the wind regime, the scatter of σ_w in the above canopy-space was plotted against the sub-canopy for day and night periods (Fig. 2). Time periods with global radiation exceeding 20 Wm^{-2} above the main tree canopy were classified as daytime, while those with lower values were considered night-time. The scatter plot was then divided into bins based on the mean of every 150 points within the scatter plot. The Pettitt (1979) test was employed to detect the weak-wind thresholds for both day and night periods. The final wind regime for the study site was determined based on the times when at least two of the three EC systems at the sub-canopy exhibited similar regimes (Fig. 2). The weak-wind threshold of σ_w was determined to be 0.34 m s^{-1} for both the main and road towers during day and night (Fig. 2a–c).

2.6. Random forest modeling of scalar gas variability

Random Forest (RF) is an established machine learning method and offers the advantage of capturing complex, non-linear relationships between the target and predictors by utilizing an ensemble of decision trees independently grown on random data subsets. We utilized the RF algorithm (Breiman, 2001) using python package RandomForestRegressor in sklearn (Pedregosa et al., 2011) to determine the importance weighting of the predictor variables outlined in Table 1 which contains a set of micrometeorological variables, turbulence metrics, wind properties, and temperature. The target variables, $\widehat{\sigma}_{CO_2}$, $\widehat{\sigma}_{CH_4}$, and $\widehat{\sigma}_{H_2O}$ were derived from GCSN using horizontal and vertical inlets with 10-minute data as described earlier. Separate models were trained for each tower in the sub-canopy and across the strong and weak wind regimes resulting in six distinct modeling scenarios. For each scenario, data were randomly split into training (80 %) and testing (20 %) subsets. Feature scaling was applied independently to training and test sets using StandardScaler and hyperparameter tuning was performed via 10-fold cross-validation using GridSearchCV. To assess the contribution of each predictor, we employed permutation importance, calculated as the mean decrease in model performance (R^2) when individual features were randomly shuffled. Importance scores were averaged over 10 permutations, and standard deviations were computed as uncertainty estimates.

2.7. Classifying FODS temperature profile using k-means

The k-means algorithm is a popular clustering method that divides n observations into k clusters. Each observation is assigned to the cluster whose mean (centroid) is closest to it. The algorithm refines these centroids iteratively and assigns observations to clusters based on their proximity to these centroids (Jain, 2010). In this study, we used the k-means to cluster the FODS temperature profiles for the strong- and weak-wind regimes and assessed the role of thermal stratification on scalar gas spatial variability. The FODS temperature is converted to potential temperature before feeding into the k-means algorithm. The potential temperature (θ) expressed as:

$$\theta = T_{FODS}\left(\frac{P_0}{P}\right)^k \quad (1)$$

where P is the air pressure in kPa, $P_0 = 100$ kPa is the reference pressure, and k is the Poisson constant assumed to be 2/7. This transformation ensures that the temperature used in the clustering process appropriately reflects the atmospheric conditions by adjusting for pressure effects.

Table 1
The predictor variables used in the RF algorithm were derived from 10-minute interval data collected at four tower locations: the main tower, road tower, hill tower, and flux tower. Vertical wind shear (dU/dz) was calculated as the difference in scalar wind speed between the upper and lower measurement heights, divided by the vertical distance between them. The wind direction shift (Δφ) represents the divergence in wind direction between the sub-canopy and above-canopy layers.

Variable	Unit	Mean ±Std main tower	Mean ±Std road tower	Mean ±Std hill tower	Mean ±Std flux tower
Turbulent Kinetic Energy (TKE)	$m^2\ s^{-2}$	0.08 ± 0.08	0.09 ± 0.08	0.16 ± 0.17	1.37 ± 1.33
Mean vertical wind (w)	m s^{-1}	−0.01 ± 0.03	0.01 ± 0.03	0.02 ± 0.10	0.08 ± 0.16
Std deviation of vertical wind (σ_w)	m s^{-1}	0.10 ± 0.05	0.11 ± 0.06	0.17 ± 0.11	0.60 ± 0.33
Std deviation of horizontal wind ($\sigma_{u,\ H}$)	m s^{-1}	0.36 ± 0.20	0.37 ± 0.21	0.50 ± 0.30	1.37 ± 0.76
Momentum flux ($\overline{u'w'}$)	$m^2\ s^{-2}$	0.00 ± 0.01	−0.01 ± 0.01	−0.01 ± 0.02	−0.38 ± 0.40
Stability parameter ($\zeta = z/L$)	-	0.33 ± 2.00	0.70 ± 4.50	0.88 ± 4.01	0.09 ± 0.91
Wind shear (dU/dz)	s^{-1}	−0.09 ± 0.04	−0.09 ± 0.04	−0.08 ± 0.04	-
Wind speed (U)	m s^{-1}	0.76 ± 0.38	0.69 ± 0.34	0.89 ± 0.51	3.23 ± 1.46
φ (Wind direction)	degrees (°)	137± 79	133 ± 83	136± 88	169± 74
Wind direction shift (Δφ)	degrees (°)	36± 45	38 ± 41	43 ± 41	-
Mean air temperature (T)	K	13.96 ± 4.83	14.32 ± 4.75	13.98 ± 4.90	14.26 ± 4.43
Std of air temperature (σ_T)	K	0.15 ± 0.08	0.19 ± 0.11	0.23 ± 0.13	0.25 ± 0.15

3. Results and discussions

This section presents the results and discussion of the study. It begins with an analysis of forest micrometeorological conditions during the LOEWE20 experiment. Subsequently, it examines the scalar gas mixing ratios and their spatio-temporal variability. The results of the machine learning analysis are then presented to identify the key drivers of this variability. Finally, the variability patterns are further investigated using FODS temperature and wind profile measurements, applying a clustering approach to characterize dominant flow and thermal regimes.

3.1. Forest microclimate during the LOEWE20 experiment

During the LOEWE20 experiment, air temperature ranged from 3.2 °C to 26.3 °C and median being between 13.7 °C to 14.2 °C with sub-canopy and above-canopy temperatures exhibiting similar variability

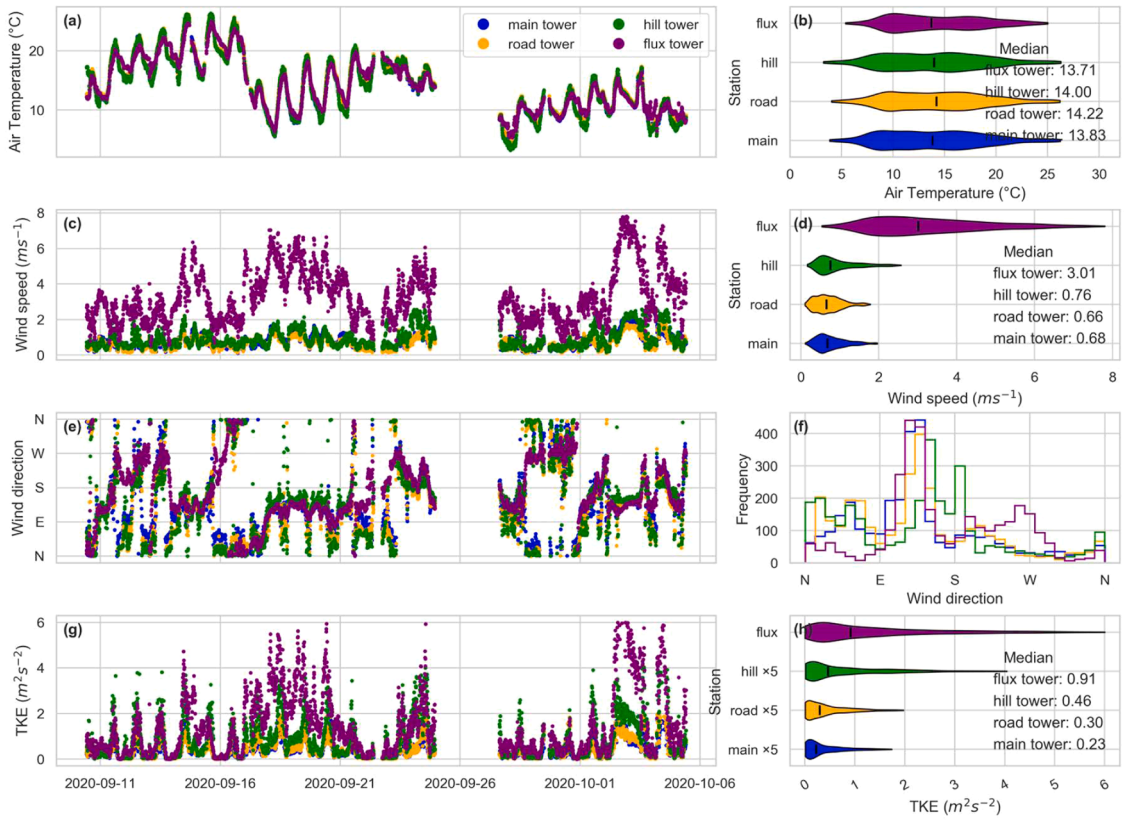

Fig. 3. Overview of time series and violin plots of (a, b) air temperature, (c, d) wind speed (g, h) turbulent kinetic energy, and (e, f) time series and histogram of wind direction during the LOEWE20 experiment, representing measurements from the sub-canopy and above-canopy. The flux tower is located above the canopy, while the other three stations are situated within the sub-canopy. In g, and h the TKE in sub-canopy was multiplied by 5 to make the plots more visible.

(Fig. 3a, and b). The median scalar wind speed (U) was between 0.7 and 0.8 ms^{-1} in the sub-canopy and 3 ms^{-1} above the canopy. The hill tower has higher wind speeds and exhibits a different wind speed distribution compared to the other two sub-canopy stations due to its more open canopy structure and its location near the southwestern edge of the forest (Fig. 3c and d). Similar to wind speeds in the sub-canopy, TKE was significantly lower compared to that above the canopy ranging up to 6.01 m^2s^{-2} for above canopy and up to 0.81 m^2s^{-2} for sub-canopy with a median of 0.23 to 0.46 m^2s^{-2} in sub-canopy and 0.96 m^2s^{-2} above-canopy (Fig. 3g and h).

The dominant wind direction was south-easterly in both the sub-canopy and above-canopy (Fig. 3e and f). In the sub-canopy, the secondary dominant wind direction was from the north and north-east, while in the above-canopy, it was from the west. The observed wind directions are consistent with the prevailing wind directions reported by Thomas and Foken (2007). Based on the weak-wind regime definition in Section 2.5, 76 % of the data collected during the LOEWE20 experiment were classified as strong-wind conditions, while 24 % were classified as weak-wind. Additionally, the occurrence of strong winds is primarily confined to the diurnal period, manifesting predominantly between the hours of 09:00 and 16:00. During nocturnal periods, wind conditions exhibit variability, ranging from weak to strong, with weak winds being more prevalent. The periods from 02:00 to 05:00 in the early morning and from 17:00 to 20:00 during the evening transition are characterized by weak-wind conditions (Fig. 3d).

During strong wind regimes, the polar plots of wind speed at sub-canopy stations indicate that higher wind speeds predominantly originate from the south, southwest, and southeast. In contrast, lower wind speeds are associated with winds coming from the north, northwest, and northeast. A similar distribution pattern is observed at the above-canopy station. Under weak-wind regimes, wind speeds are more evenly distributed across all directions at both sub-canopy and above-canopy levels (Fig. 4a-d). The mean vertical potential temperature profile observed with FODS under strong-wind conditions exhibits a similar structure to that of the full observation period, with a maximum temperature of 14.2 °C occurring at a height of 22 m. This profile structure is consistent with earlier findings by Raupach (1989) and Schilperoort et al. (2020).

The lower canopy (below 5 m) remains stably stratified in both strong- and weak-wind regimes, with a vertical temperature difference (ΔT) of 0.9 K during strong winds and 2.4 K during weak winds. In contrast, the upper portion of the profile shows increased temperatures, indicating stronger vertical gradients and reduced mixing above the subcanopy (Fig. 4e, and f).

The wind speed profiles in both strong- and weak-wind regimes exhibit a pronounced vertical gradient caused by the drag exerted by the forest canopy. Wind speeds are higher above the canopy and decrease sharply within the subcanopy due to momentum absorption by leaves and branches. Notably, the profiles display a local maximum at around 3 m and a minimum at approximately 11 m in both regimes, a pattern consistent with findings from previous studies such as Thomas and Foken (2007) and Rodrigues et al. (2021).

The diurnal course of carbon dioxide flux (F_{CO2}) across the vertical forest profile revealed a pronounced contrast between above-canopy (Fig. 5a) and sub-canopy (Fig. 5b–d) eddy covariance stations. At the above-canopy site, F_{CO2} reflects the ecosystem exchange, with the strong wind regime exhibiting a high diurnal amplitude: daytime net ecosystem exchange dominated by photosynthetic uptake peaked at approximately –30 μmol m^{-2} s^{-1} and nocturnal respiratory efflux around −10 μmol m^{-2} s^{-1}. By comparison, the weak regime shows markedly dampened fluxes, indicating that under low-turbulence conditions, vertical CO_2 transport is suppressed. Within the sub-canopy, fluxes at the main (b), road (c),

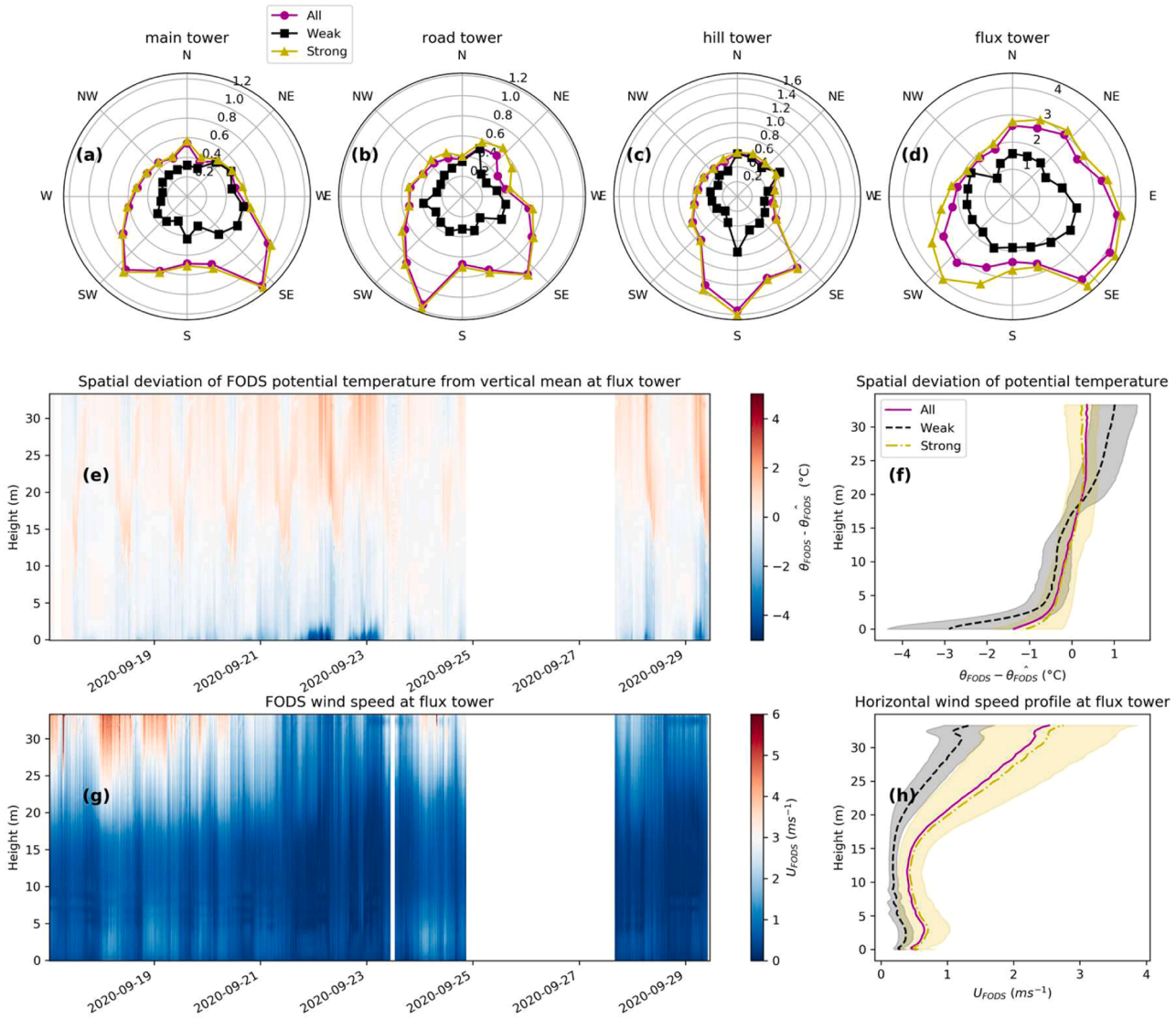

Fig. 4. Polar plots of scalar wind speed for the main, road, hill, and flux towers are shown in panels (a–d), separated by weak and strong wind regimes. Panel (e) presents the spatial deviation of FODS-derived temperature time series at the flux tower, while panel (f) displays the corresponding temperature spatial deviation profiles averaged by wind regime. Panel (g) shows the distributed FODS wind speed, calculated following (van Ramshorst et al., 2020), and panel (h) presents the vertical wind speed profiles averaged by wind regimes. All data presented in this graph were 10-minute averages. Shaded areas in f and h show the variability (± 1 standard deviation) of the mean values.

and hill (d) towers are roughly an order of magnitude smaller, consistent with decoupling of the forest floor. The strong coupling regime exhibits relatively stable, low-magnitude fluxes, whereas the weak regime is punctuated by transient peaks particularly around 09:00 and 15:00 in panels (b) and (c). These peaks correspond to "flushing" events, triggered by the breakdown of the nocturnal temperature inversion in the morning, which temporarily enhances vertical mixing and CO_2 transport. We focused this additional flux analysis on CO_2 exchange rather than on sensible heat (H) or latent heat (LE). CO_2 is the only scalar considered with a substantial and well-defined source within the forest subcanopy, as roughly two-thirds of ecosystem respiration originates from soil respiration at the forest floor.

3.2. Sub-canopy scalar gas mixing ratios

At the horizontal inlets CO_2 mixing ratios ranging from 394 to 425 ppm were measured, while vertical inlets recorded a broader range from 394 to 491 ppm, based on the 5th and 95th percentiles, respectively. CO_2 mixing ratio indicates a relatively uniform horizontal distribution, in contrast to a vertical gradient with accumulation near the forest floor which decreases with height (Table 2). CO_2 mixing ratios remained consistent over time across both horizontal and vertical inlets, with the exception of inlet S10, located 10 cm agl. S10 exhibited persistently higher mixing ratios, driven by soil autotrophic and heterotrophic respiration. These elevated levels were especially prominent during night-time, when weak-wind conditions and stable stratification in the subcanopy suppress turbulence and inhibit vertical mixing (see time series in Appendix Fig. A5a). The diurnal evolution of vertical profiles show vertical gradient, with CO_2 mixing ratios peaking near the ground and decreasing with height during night-time, then becoming more mixed during daytime. In contrast, the horizontal inlets showed minimal variation in CO_2 mixing ratio across locations, following a consistent diurnal pattern with lowest values occurring around 13:00 and highest mixing ratios during the early night-time hours (Fig. 6a and b). This buildup results from ecosystem respiration accumulating under weak-wind and stably stratified conditions with suppressed turbulent mixing. As daytime heating initiates the development of a convective turbulent boundary layer, buoyancy-driven turbulence intensifies,

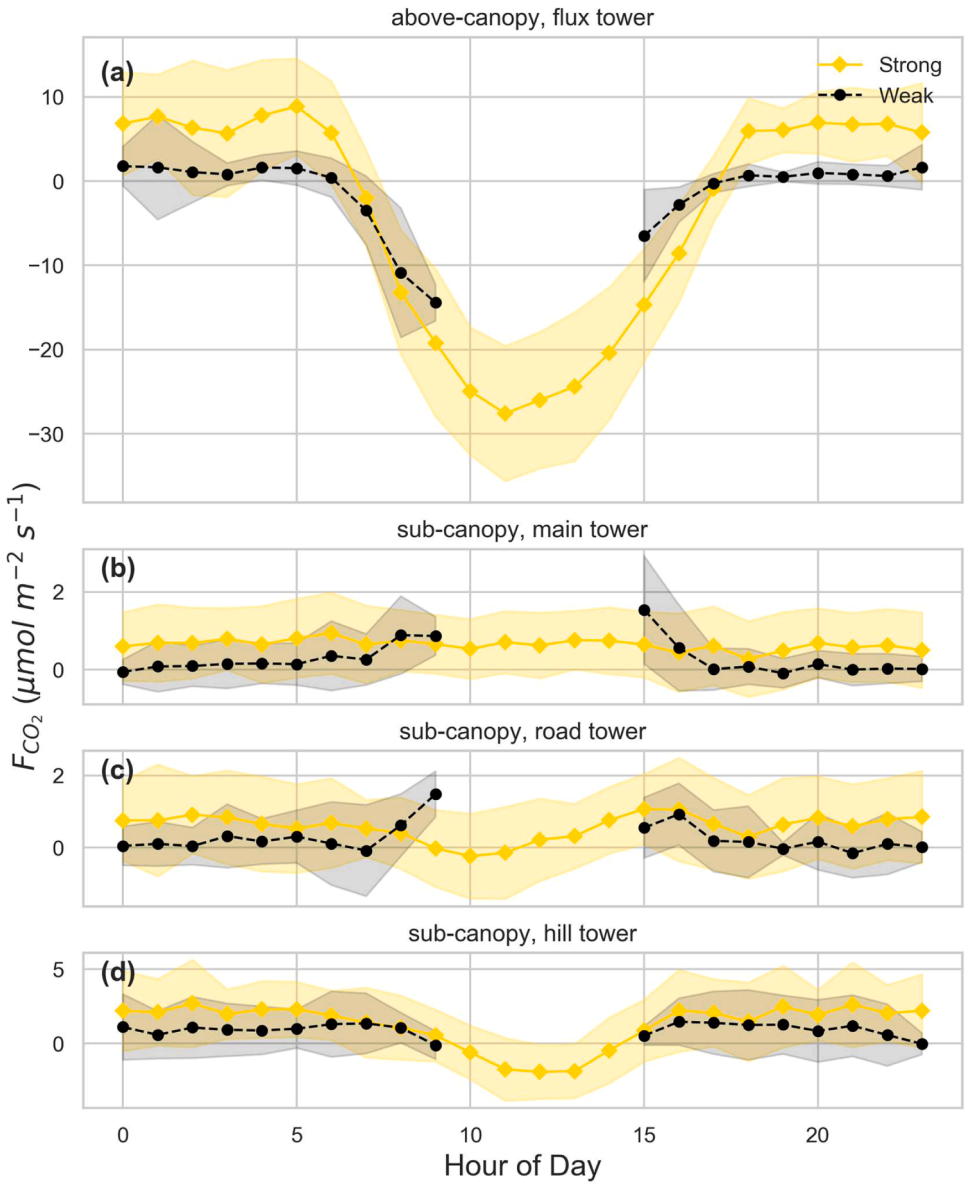

Fig. 5. Diurnal course of carbon dioxide flux (F_{CO2}) for above- and sub-canopy eddy covariance stations, separated into strong and weak regimes. Shaded areas indicate ±1 standard deviation around the mean.

generating large eddies that interact with the canopy top. The upper canopy acts as a momentum sink, absorbing energy and producing shear-driven turbulence in the canopy-top shear layer. This turbulence can be transported downward, especially through canopy gaps or more open understory areas, enhancing vertical mixing within the subcanopy. The resulting increase in turbulent exchange reduces CO_2 accumulation near the ground by facilitating more efficient transport (Raupach et al., 1996; Thomas et al., 2013; Vickers and Thomas, 2014).

CH_4 mixing ratios were found to fall within the range of 1891 to 2036 ppb for 5th and 95th percentiles consistent with similar studies like (Song et al., 2024; Sundqvist et al., 2015) showing subtle differences across horizontal inlets and stronger gradient in vertical inlets (Table 2). In contrast to CO_2, the CH_4 mixing ratio at the ground is the lowest among all inlets, which supports the observation of a forest soil as a sink of methane for temperate forests (Dutaur and Verchot, 2007). The main factors influencing methane dynamics in forest ecosystems are soil moisture, soil nutrients such as carbon, nitrate, and phosphorus, and natural disturbances such as drought and fire (Feng et al., 2020). Accordingly, the observed sharp peaks mostly occur after precipitation events, displacing the CH_4 in soil pores (Fig. A5b). The diurnal cycle of the CH_4 mixing ratio peaked during the nighttime for both horizontal and vertical inlets (Fig. 6c, and d) when the weak-wind regime dominated and the lowest mixing ratio occurred during the day in the late afternoon similar to the diurnal courses observed in (Botía et al., 2020; Harazono et al., 2015; Querino et al., 2011). The observed increase in CH_4 mixing ratio with height (i.e., lower near the forest floor and higher aloft) implies a positive vertical gradient ($\partial CH_4/\partial z > 0$). According to flux-gradient similarity theory, this corresponds to a downward turbulent flux of CH_4, assuming near-neutral stratification and sufficient turbulence and suggests that the forest floor is a net sink of CH_4 (Borken et al., 2006; Krebs et al., 2024; Ni and Groffman, 2018). The secondary minimum in CH_4 mixing ratios around 05:00 is attributed to wind regime . During this period, an increased frequency of weak-wind events suppresses the downward transport of CH_4 from above the canopy to lower layers (Fig. 2d). Furthermore, the night-time shift in sub-canopy wind direction—from approximately 135° at 01:00 to 105° at 03:00 modifies the source area influencing CH_4 mixing ratios, contributing to the observed minimum.

Table 2
Statistics of scalar gas mixing ratios observed with GCSN during the LOEWE20 experiment, the diurnal courses of which is presented in Fig. 6. The values for p5, p50, and p95 represent the 5th percentile, median, and 95th percentile, respectively. Each column is color-coded from blue to red, representing low to high values.

		CO_2 (ppm)				CH_4 (ppb)				H_2O (ppth)			
Inlets		**p5**	**p50**	**mean**	**p95**	**p5**	**p50**	**mean**	**p95**	**p5**	**p50**	**mean**	**p95**
S1	Horizontal inlets at 4m	395	406	407	422	1924	1986	1982	2034	8.06	12.51	12.27	16.28
S2		394	407	408	425	1925	1987	1983	2035	8.13	12.62	12.34	16.34
S3		395	407	407	421	1926	1986	1983	2035	8.29	12.57	12.33	16.26
S4		395	407	408	422	1925	1987	1983	2036	8.15	12.58	12.32	16.25
S5		395	407	407	422	1924	1986	1982	2034	8.17	12.63	12.36	16.35
S6		395	408	409	425	1924	1985	1982	2035	8.18	12.65	12.40	16.48
S7		395	407	408	422	1925	1986	1982	2034	8.23	12.57	12.35	16.34
S8		395	407	408	425	1924	1985	1982	2035	8.21	12.61	12.36	16.32
S9, 32m	Vertical inlets	394	403	404	418	1928	1989	1985	2036	8.05	12.41	12.13	15.98
S11, 23m		394	404	405	418	1927	1989	1985	2036	8.14	12.47	12.21	16.10
S12, 4m		395	410	410	425	1923	1984	1981	2034	8.37	12.66	12.43	16.51
S13, 2.5		395	410	410	427	1923	1983	1980	2033	8.30	12.65	12.44	16.52
S10, 10 cm		398	426	433	491	1891	1968	1964	2030	8.60	12.93	12.84	17.39

The time series of water vapor mixing ratios from both vertical and horizontal inlets exhibit a consistent fluctuation (Fig. A5c), with values ranging between 8.05 and 17.39 ppth for the 5th and 95th percentiles, respectively (Table 2). The horizontal inlets generally show an even distribution of H_2O mixing ratios, with the exception of inlets S6, S12, and S13. These inlets are positioned in more open canopy areas, where increased solar radiation leads to enhanced subcanopy evapotranspiration (ET). The vertical profile shows a negative gradient with decreasing H_2O mixing ratios with height. Similar to the CO_2 mixing ratio patterns, water vapor tends to accumulate near the forest floor due to stable stratification and suppressed turbulent mixing (Table 2).

The diurnal variation in H_2O mixing ratio closely follows the patterns of solar radiation and vapor pressure deficit (VPD), consistent with findings by Shen et al. (2015). As solar radiation and air temperature rise from early morning, ET increases, leading to elevated H_2O mixing ratios that typically peak between 10:00 and 12:00. In the afternoon, despite continued increases in temperature, the H_2O mixing ratio declines (Fig. 6e and f), due to intensified turbulent mixing under stronger wind conditions, which enhances vertical transport of water vapor from the sub-canopy. An exception is observed at inlet S10, where a pronounced accumulation of water vapor occurs near the ground in the absence of significant turbulence. This inlet displays a stronger diurnal amplitude compared to others, with its maximum coinciding with a marked reduction in scalar wind speed in the sub-canopy between 16:00 and 17:00. Additionally, delayed soil temperature peaks typically 2–4 h after the air temperature maximum could contribute to the later peak in forest floor ET by increased evaporation relative to that from upper canopy layers (Ruehr et al., 2010).

3.3. Spatial variability of scalar gas concentrations

As demonstrated in Fig. 7a and g, the vertical $\widehat{\sigma}_{CO_2}$ displays a greater range in comparison to the horizontal, with a mean of 10.8 and 2 ppm, respectively. High $\widehat{\sigma}_{CO_{2,\,v}}$ can be attributed to the greater temporal variability in CO_2 vertical profiles, as demonstrated in Fig. 7a. The $\widehat{\sigma}_{CO_{2,\,h}}$ is considered to be a consequence of the alteration of wind field and the shuffling of wind direction between different sources, specifically the south-easterly winds in the subcanopy and easterly winds above the canopy. (Fig. A6d, j, p, and v). The subscripts *v* and *h* in $\widehat{\sigma}_{\chi}$ denote the vertical and horizontal spatial variability of the scalar gas χ.

The diurnal cycle of $\widehat{\sigma}_{CO_2}$ exhibits a similar diurnal pattern to mean CO_2 mixing ratio in both vertical and horizontal inlets. $\widehat{\sigma}_{CO_2}$ increases during nocturnal periods and decreases for daylight conditions, coinciding with the development of a turbulent boundary layer within the forest. It is evident that the wind regime also plays a significant role during nocturnal periods, as evidenced by the increase in $\widehat{\sigma}_{CO_2}$ during periods of weak-wind and subsequent decrease during periods of strong wind (Fig. 7d). In contrast, the wind regime does not separate the diurnal course of horizontal $\widehat{\sigma}_{CO_2}$, with the exception of the morning and evening transition periods, during which $\widehat{\sigma}_{CO_2}$ exhibits a maximum.

The mean $\widehat{\sigma}_{CH_4}$ across all wind regimes ranges between 1.9 and 7.8 ppb for horizontal and vertical inlets, respectively. A notable peak in the vertical diurnal cycle of $\widehat{\sigma}_{CH_4}$ is evident during periods of weak wind, specifically for the early morning transition (EMT) and late afternoon transition (LAT) times, as illustrated in Fig. 7e. $\widehat{\sigma}_{CH_{4,\,h}}$ shows minor variations, indicating that methane is predominantly well-mixed in the horizontal plane at a depth of 4 m (Fig. 7k). It is interesting to note that $\widehat{\sigma}_{CH_{4,v}}$ does not match the diurnal pattern of CH_4 mixing ratio, but rather is more similar to the diurnal evolution of spatial standard deviations of CO_2. This finding suggests that the vertical spatial variability of CH_4 mixing ratio is driven by mechanical shear in sub-canopy. As illustrated in Fig. 7f, the peak of TKE coincidences with minimum $\widehat{\sigma}_{CH_4}$. It is evident that, in consideration of the wind direction, during periods of strong wind regimes, the $\widehat{\sigma}_{CH_4}$ magnitudes show a lack of sensitivity to wind direction. Conversely, for the weak wind regime, sub-canopy northerly and north-easterly winds contribute substantially to $\widehat{\sigma}_{CH_4}$.

Similar to $\widehat{\sigma}_{CO_2}$ and $\widehat{\sigma}_{CH_4}$, $\widehat{\sigma}_{H_2O}$ exhibits a greater variability in the vertical direction than in the horizontal with mean values of 0.27 and 0.11 ppth, respectively (Fig. 7c and i). It is, however, markedly higher during the daytime and lower at night for both vertical and horizontal inlets. Under weak-wind conditions, vertical inlets show pronounced variability during the evening transition period (Fig. 7f and l). Notably, the $\widehat{\sigma}_{H_2O,\,h}$ peaks concurrently with global radiation (Q_s*), suggesting that spatial heterogeneity in canopy density and differential solar heating of the forest floor and subcanopy vegetation lead to varying ET rates and, consequently, greater variability. In contrast, the $\widehat{\sigma}_{H_2O,\,v}$ peak does not coincide with peak of either TKE or Q_s*. This might be

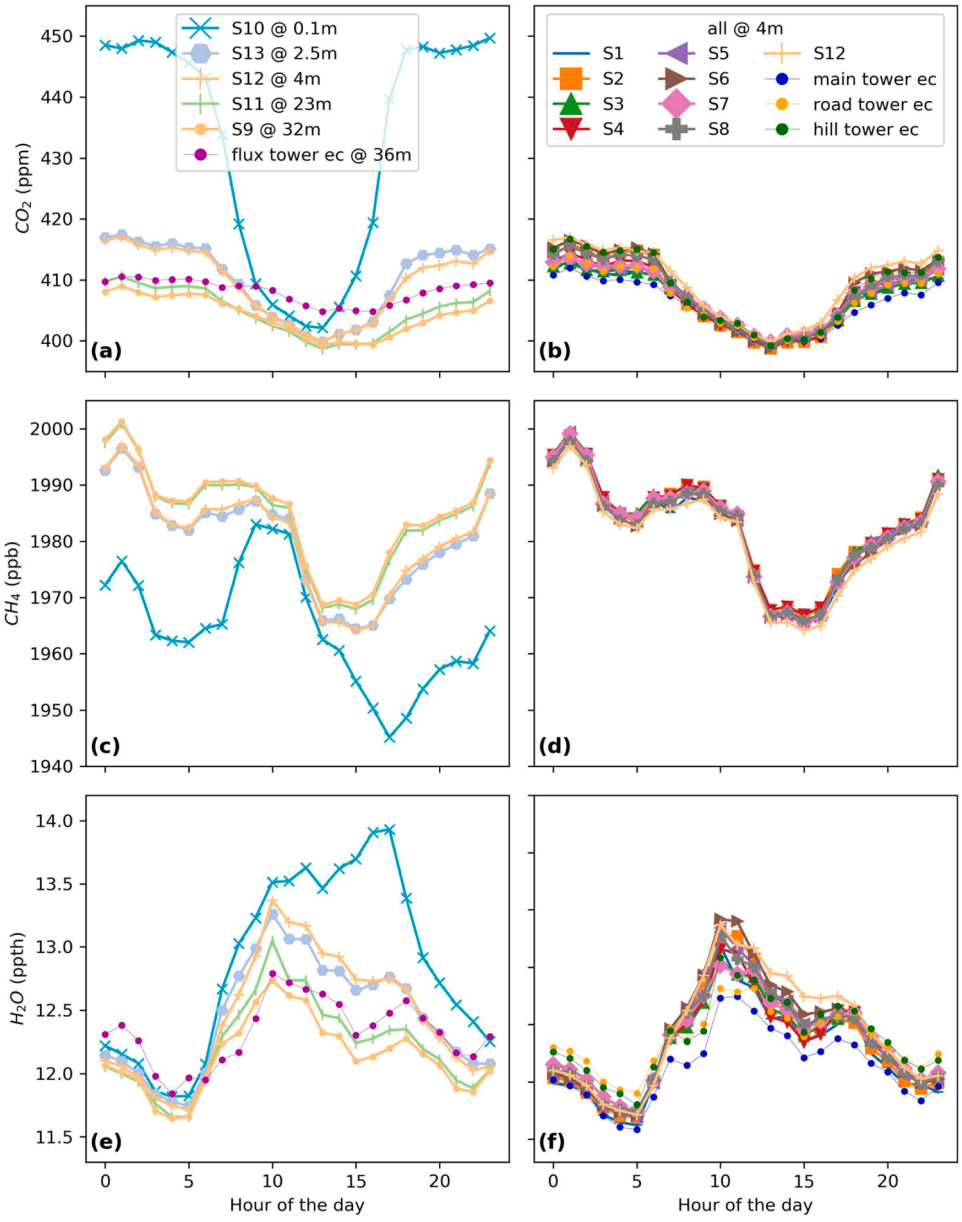

Fig. 6. Diurnal course of scalar gas mixing ratios in the vertical profile (a, c, and e) and horizontal (b, d, and f) including eddy covariance measurements computed based on 10-minute data averaged over study period in different hours of the day.

attributed to magnitude of ET which reaches to its diurnal maximum with 2–3 h later than TKE and Q_s*.

3.4. *Drivers of spatiotemporal variability of greenhouse gases*

To investigate the drivers of greenhouse gas variability in the sub-canopy, we consider three groups of potential drivers: statistics of turbulence, the mean flow, and air temperature (Table 1). The scatterplots in Fig. A7 illustrate an example of the variation of the chosen micrometeorological variables for $\widehat{\sigma}_{CO_{2,\ v}}$ at the hill tower, demonstrating a nonlinear relationship between the micrometeorological variables and $\widehat{\sigma}_{CO_{2,v}}$. RF model is employed to assess the contribution of each variable to modelling the spatial standard deviation of greenhouse gases.

Permutation feature importance analysis for both vertical and horizontal $\widehat{\sigma}_{CO_2}$ under strong-wind regimes reveals that the MOST dynamic stability parameter of sub-canopy (ζ), TKE, and σ_w are the dominant predictors. This indicates that turbulence-driven processes largely govern the variability of $\widehat{\sigma}_{CO_2}$ during strong-wind conditions (Figs. 8a and 9a). In contrast, under weak-wind conditions, air temperature driven by absorbed solar radiation emerges as the most influential variable in explaining both vertical and horizontal $\widehat{\sigma}_{CO_2}$ (Figs. 8b and 9b). This underscores the critical role of temperature in modulating mixing processes during weak-wind periods, which frequently occur at night due to radiative cooling and reduced mechanical turbulence. The result is generally consistent with expectations from nocturnal boundary-layer theory, yet it is reassuring to see this pattern quantitatively confirmed by the statistical analyses.

For $\widehat{\sigma}_{CH_{4,v}}$, temperature is also a primary predictor in both wind regimes (Figs. 8c), with turbulence metrics being of secondary importance during strong-wind periods. However, the behavior of horizontal $\widehat{\sigma}_{CH_{4,\ h}}$ differs: under strong-wind conditions, its variability is primarily driven by σ_w and vertical wind shear (dU/dz), under weak-wind conditions, the horizontal $\widehat{\sigma}_{CH_4}$ is best explained by the scalar wind speed (U) (Figs. 9c and 9d). Since σ_w is typically influenced by bulk shear (e.g., U) and is not included as a predictor here, it can be argued that during weak-wind conditions, turbulence is not primarily driven by bulk shear

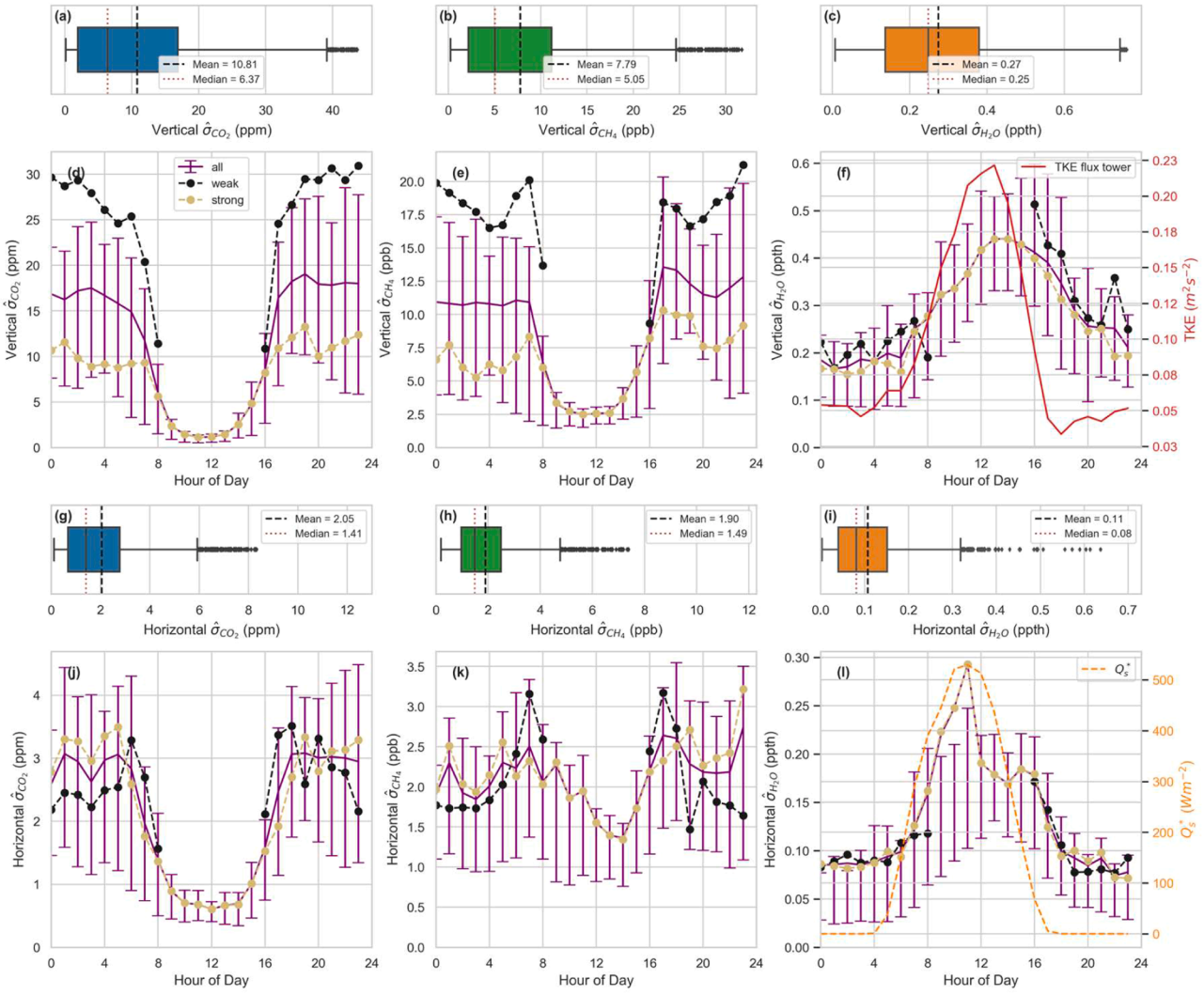

Fig. 7. Boxplots of the spatial standard deviations of CO_2, H_2O, and CH_4 mixing ratios ($\hat{\sigma}_{CO_2}$, $\hat{\sigma}_{CH_4}$, and $\hat{\sigma}_{H_2O}$) are shown for the vertical (a–c) and horizontal (g–i) inlets, alongside their respective diurnal cycles in the vertical (d–f) and horizontal (j–l) under weak and strong wind regimes. Error bars in the diurnal plots and width of boxes represent the interquartile range (IQR, 25th to 75th percentiles). The whiskers extend to 1.5 IQR, and outliers beyond this range are plotted individually. Mean and median values are marked as dashed and dotted lines to highlight asymmetries in the distribution. The diurnal course of TKE in flux tower were added to subplot (f) and global radiation (Q^*_s) to subplot (l) for comparison.

but site-dependent non-stationary motions (Mahrt et al., 2015). Furthermore, U and wind direction being important predictors of $\hat{\sigma}_{CH_{4,h}}$, highlight the influence of horizontal advection processes within the subcanopy.

We note that other potential driver such as soil moisture and soil temperature can significantly influence CH_4 fluxes in forest sub-canopy (Krebs et al., 2024). These factors may contribute to the spatial variability of CH_4 mixing ratios; however, the temperature variation in these autumn months is relatively small compared to summer and is therefore expected to have only a smaller effect on the explanatory power of the models for CH_4 dynamics.

Figs. 8e, f and 9e, f demonstrate the dominant role of temperature in explaining the variability of $\hat{\sigma}_{H_2O}$ across wind regimes and both vertical and horizontal directions. For $\hat{\sigma}_{H_2O,\ h}$, temperature remains the most important variable, reinforcing observations discussed in Section 3.3. There, we attributed spatial variability in ET to heterogeneity in subcanopy radiation caused by variable canopy cover, which results in ground-level temperature differences. These differences affect ET rates and thus horizontal variability in H_2O mixing ratio. However, such spatial heterogeneity cannot explain $\hat{\sigma}_{H_2O,\ v}$ variability, as vertical sampling inlets are collocated on a single tower. In this case, the importance of temperature reflects its direct control over ET processes across vertical canopy layers, each with different available energy. For instance, the available energy at the ground differs substantially from that of the canopy crown, leading to variability in canopy crown transpiration. Furthermore, coherent structures, the primary mechanism driving canopy transport, can also influence the variability of greenhouse gas concentrations within the canopy (Thomas and Foken, 2007b).

3.5. *Comparing FODS temperature profiles to spatiotemporal variability of greenhouse gas concentrations*

The vertical profiles of FODS potential temperature at the flux tower was used to analyse the role of thermal stratification in the forest canopy on scalar gas mixing, as the temperature profile will respond to changes in wind shear induced mixing and solar radiation. These vertical profiles were then fed into the k-means algorithm to cluster the data, resulting in three clusters for each wind regimes, as shown in Fig. 10a and b. Each cluster under strong-wind conditions can be described as follows. Cluster 1 predominantly occurs during the daytime on sunny days, when the canopy crown absorbs solar radiation heating up the air while the

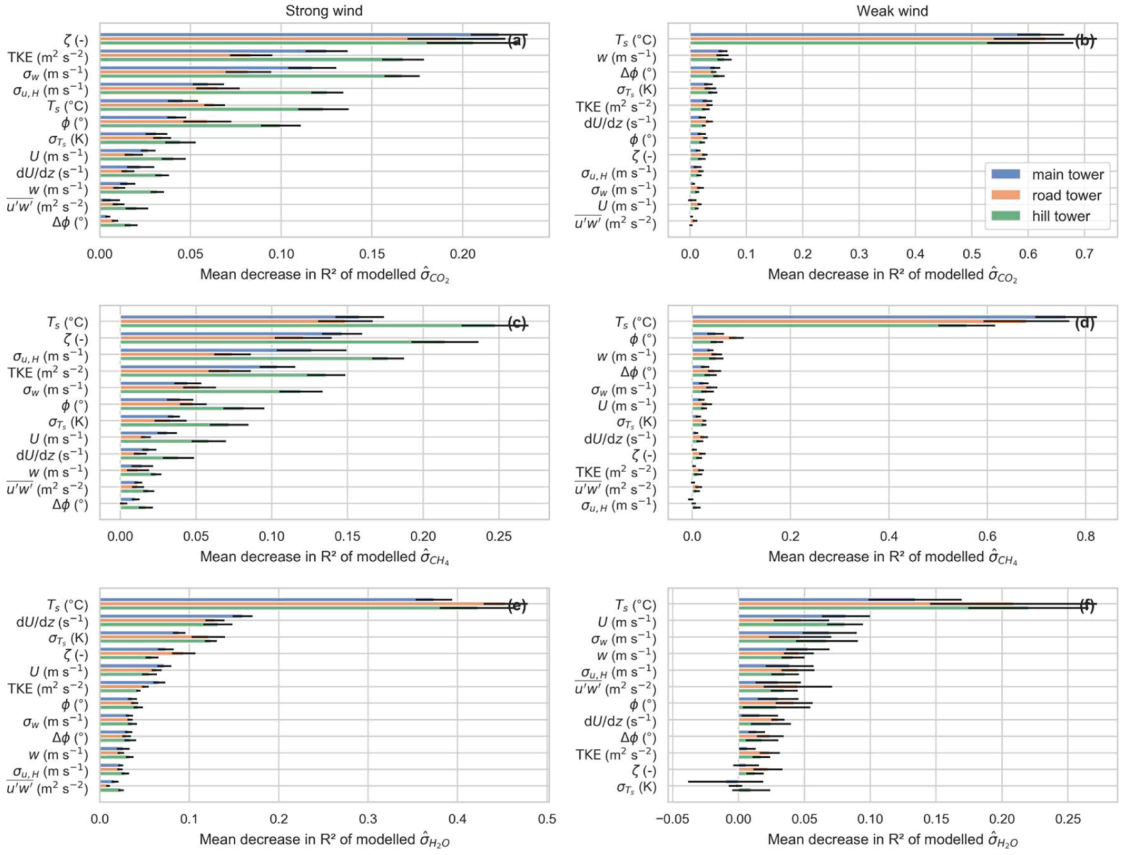

Fig. 8. Random forest feature importance of micrometeorological variables in modeling the vertical standard deviation of CO_2, CH_4, and H_2O under strong- and weak-wind regimes at main, road, and hill towers, including vertical wind shear (dU/dz) and wind direction shift (Δφ) derived from sub- and above-canopy stations. The length of each bar represents the mean importance score, indicating the relative contribution of each feature to model performance, while error bars (± Std) reflect variability across 10 permutation repetitions.

sub-canopy remains relatively cool. This results in a modest warming of the upper understory (at heights between 10 and 15 m) and the development of unstable stratification within the densest part of the canopy (at heights between 15 and 25 m). Cluster 2 primarily occurs during night-time, driven by radiative cooling of both the canopy and forest floor, leading to stable stratification near the ground and weakly stable conditions at canopy height. Cluster 3 is mainly associated with morning and evening transition periods and is characterized by stable stratification near the ground and near-neutral conditions at canopy height. This regime typically develops under cloudy conditions, which inhibit significant heating of the canopy.

During strong-wind conditions, all three clustered temperature profiles indicate statically stable stratification near the forest floor at different strengths. The distribution of event hours for each cluster is shown in Fig. 10e and f.

The clusters under weak-wind conditions can be described as follows. Cluster 4 is characterized by weaker stable stratification near the ground and above the canopy, with near-neutral conditions around 5 m height. This pattern develops as both the forest floor and canopy cool through longwave radiative loss. Notably, the forest floor is also subject to radiative cooling, as it can partially exchange radiation with the sky through canopy gaps. This stratification pattern predominantly occurs during nighttime including a significant number of events during the evening transition period. Clusters 5 and 6 exhibit very stable stratification within the sub-canopy and stable conditions above the canopy, driven by radiative cooling of both the forest canopy and forest floor. These clusters display a strongly stratified structure compared to the first cluster, with no indication of near-neutral stratification around 5 m height.

3.5.1. *Horizontal variability of greenhouse gas concentrations*

Cluster 2 in strong-wind conditions is the only cluster that occurs during the night (Fig. 10a and c); hence IQR range of $\hat{\sigma}_{CO_{2,\ h}}$ and $\hat{\sigma}_{CH_{4,\ h}}$ in horizontal inlets are the greatest due to higher mixing ratio of CO_2 and CH_4. The IQR and median of $\hat{\sigma}_{CO_{2,\ h}}$ and $\hat{\sigma}_{CH_{4,\ h}}$ in the two other clusters decrease with increasing horizontal wind strength at the forest floor in horizontal inlets (Fig. 11a and b, Fig. 10c). Weak-wind conditions were dominated by night-time except cluster 4 which presents calm evening transition periods, where the IQR and median of horizontal spatial standard deviation of greenhouse gases remain high. The variability among different horizontal inlets can be attributed to differences in canopy structure openness, which varies across inlets and affects the local stratification the lower subcanopy. Additionally, the evening transition period—marked by a sudden drop in TKE, reduced photosynthesis, and increased accumulation of gases—further contributes to this variability, as the transition does not occur simultaneously across the entire sub-canopy due to spatial heterogeneity in forest structure. The IQR and median values for $\hat{\sigma}_{CO_{2,\ h}}$, $\hat{\sigma}_{CH_{4,\ h}}$ in clusters 5 and 6 follow the horizontal wind speed strength as well, and the variability of all three scalar gases scales consistently with horizontal wind speed (Fig. 11d and e).

During strong-wind regimes, the highest median of $\hat{\sigma}_{H_2O,\ h}$ was observed in Cluster 1, which represents daytime conditions. This can be attributed, first, to high ET rates during sunny periods, enhancing horizontal variability in water vapor. Second, spatial variability in ET across horizontal inlets is driven by variability in solar radiation reaching the forest floor and horizontal differences, in vegetation structure contributes to this pattern (see Fig. 10e and Fig. 11c). The variability of the vegetation structure is evident in the aerial image shown in Fig. 1a,

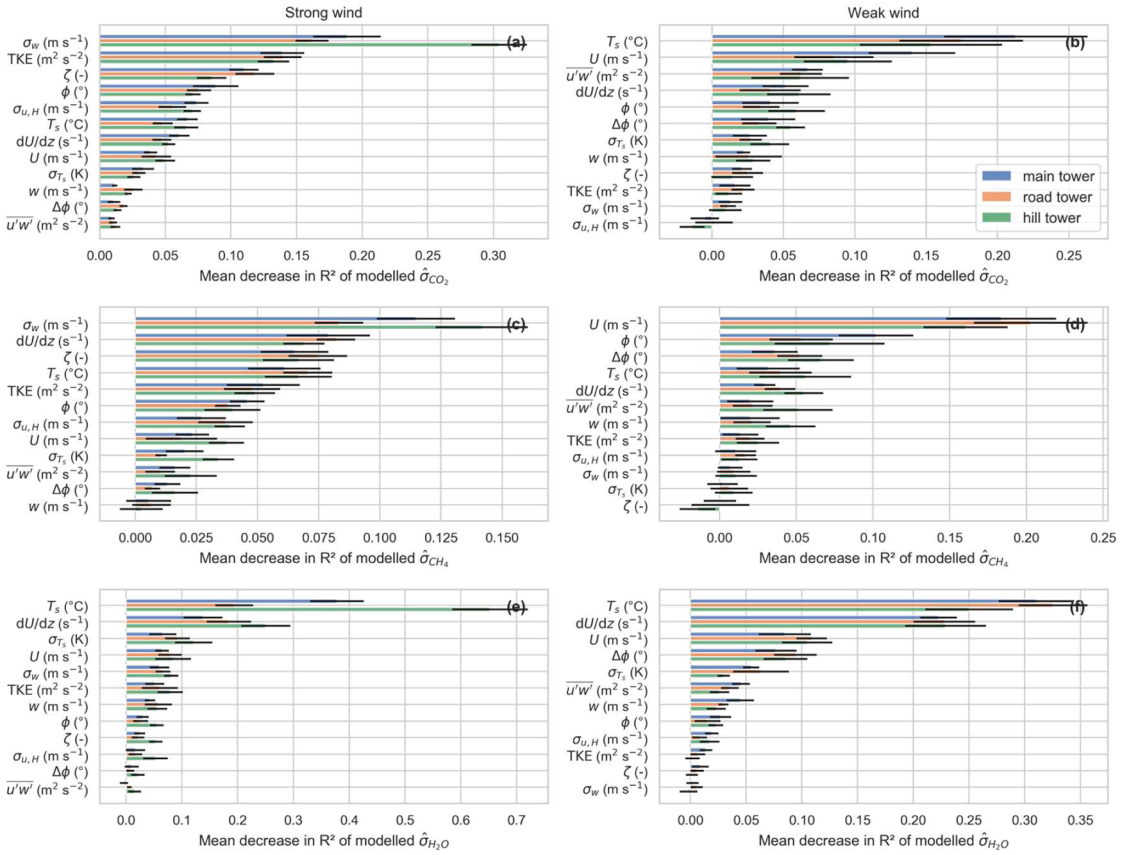

Fig. 9. Random forest feature importance of micrometeorological variables in modeling the horizontal standard deviation of CO_2, CH_4, and H_2O under strong- and weak-wind regimes at main, road, and hill towers, based on input features including vertical wind shear (dU/dz) and stability index ($\Delta\varphi$) derived from sub- and above-canopy stations. The length of each bar represents the mean importance score, indicating the relative contribution of each feature to model performance, while error bars ($\pm$ Std) reflect variability across 10 permutation repetitions.

where the southern and northeastern parts of the study area are adjacent to partially open canopy and younger trees. During weak-wind regimes, the horizontal variability of H_2O is highest in Cluster 4, which is the only cluster that includes daytime period particularly the evening transition when ET is still substantial. This variability is further enhanced by spatial heterogeneity in ET, driven by sub-canopy structural differences and uneven radiation distribution across the forest sub-canopy. Under strongly stable stratification, mixing processes are largely suppressed together with absence of ET during the night time, resulting in minimal variability in H_2O mixing ratio (Fig. 11f).

3.5.2. *Vertical variability of greenhouse gas concentrations*

The vertical variability of $\widehat{\sigma}_{CO_2}$ and $\widehat{\sigma}_{H_2O}$ under strong-wind conditions scales with the static stability of the upper canopy (above 15 m). Cluster 1, characterized by unstable stratification, shows the lowest variability, whereas Cluster 2, with stable stratification, exhibits the highest variability. Cluster 3, with near-neutral conditions, lies in between (Fig. 12a and b).

Under weak-wind conditions, Cluster 5 displays the largest IQR and median values due to very stable stratification near the ground, which suppresses mixing and leads to vertical separation of ground-emitted gases. In contrast, Cluster 4, with weaker stability near the ground and within the canopy, shows reduced IQR and median. For H_2O under strong-wind conditions, vertical variability is greatest in Cluster 1 (daytime), driven by both variability in energy and TKE, and by vertical differences in ET sources: the ground and canopy contribute significantly, while the mid-canopy adds little (Fig. 12c). During weak-wind conditions, H_2O variability is also highest in Cluster 1, which includes daytime especially the evening transition period. During this time, ET remains substantial, and near-neutral stratification in the subcanopy allows mixing between lower and upper layers, enhancing vertical spatial variability (Fig. 12f).

It can be argued that the spatial variability of CO_2 and CH_4, both horizontally and vertically, can largely be explained by the potential temperature profile alone, which integrates the effects of TKE and radiative processes into the resulting thermal stratification. In this framework, unstable or near-neutral profiles increase mixing and reduce scalar variability, while stable stratification especially near the ground or within the canopy suppresses mixing and enhances spatial gradients. For horizontal variability in CO_2 and CH_4, additional factors such as forest structural heterogeneity and local differences in leaf area index (LAI) further modulate stratification patterns and the degree of gas accumulation or dispersion across inlets. However, water vapor variability deviates from this pattern due to the fundamentally different nature of its source ET, which is tightly coupled to solar radiation, plant physiology, and surface moisture availability. Since ET occurs primarily during the daytime and can vary strongly with both vertical (ground vs. canopy crown) and horizontal heterogeneity (e.g., gaps, undergrowth), potential temperature alone is insufficient to explain water vapor variability. Instead, its variability reflects a more complicated interplay between enthalpy availability, ET dynamics, and local canopy structure, particularly during transitional periods when residual ET continues under weakly stratified conditions.

4. Conclusions

Our analysis of scalar gas measurements in the forest sub-canopy revealed distinct vertical and horizontal variabilities for CO_2, CH_4, and

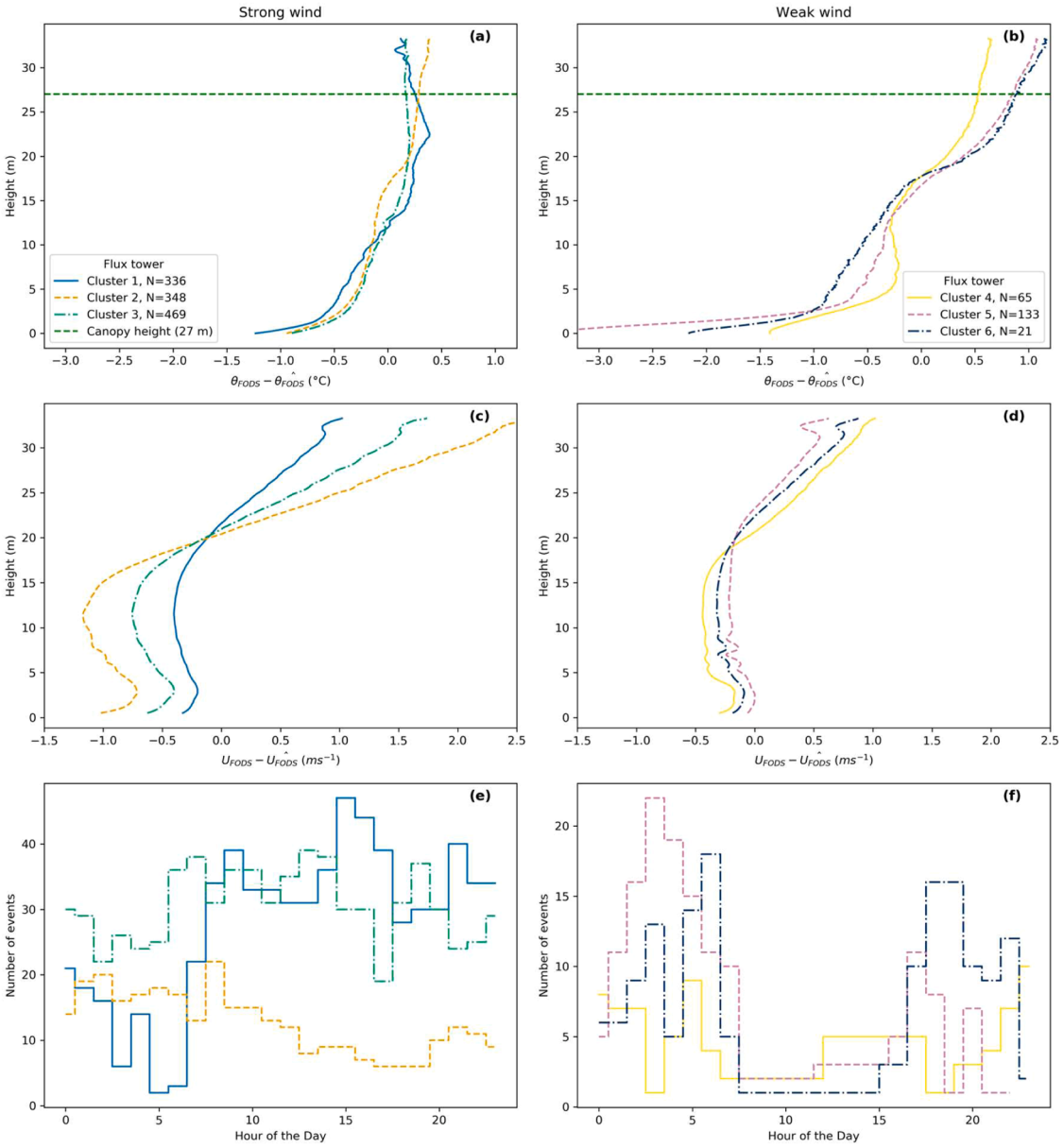

Fig. 10. Average FODS potential temperature and wind speed profiles for each cluster, normalized by subtracting the spatial mean of each profile within the cluster, under strong- (a and c) and weak-wind (b and d) conditions at the flux tower. (e) shows the distribution of event hours for each cluster during strong-wind conditions, and panel (f) during weak-wind conditions. The canopy height reference is based on.

H_2O mixing ratios, shaped by the interplay between biological processes and micrometeorological conditions. CO_2 showed strong vertical gradients, driven by nocturnal accumulation from respiration near the ground under stable stratification and weak turbulence, while CH_4 exhibited a reversed gradient compared to CO_2, consistent with soil uptake. Water vapor mixing ratios also followed a systematic vertical pattern, with accumulation near the forest floor and diurnal changes aligned with ET dynamics. Horizontal variations were notably smaller for all scalars, reflecting the homogeneous lateral distribution at 4 m height, except in areas with more open canopy, which altered the local radiation and ET balance. Diurnal and spatial variability of greenhouse gases were closely tied to wind regime and turbulence intensity: weak-wind regime enhanced vertical heterogeneity, while convective daytime turbulence led to more uniform mixing. Spatial standard deviations of scalar mixing ratios were generally higher in the vertical than the horizontal dimension. Notably, $\widehat{\sigma}_{CO_2}$ and $\widehat{\sigma}_{CH_4}$ were highest under weak-wind conditions, while $\widehat{\sigma}_{H_2O}$ peaked during the day, correlating with radiation-driven ET heterogeneity. These findings underscore the importance of capturing fine-scale spatiotemporal variability and understanding the micrometeorological drivers that govern scalar transport in complex forest environments. They also highlight the utility of dense sensor networks like GCSN for advancing process-level understanding and improving model parameterizations of trace gas exchange in forest ecosystems.

The RF analysis reveals that scalar gas variability in the forest subcanopy is governed by turbulence under strong winds and by temperature under weak winds. CO_2 variability is driven mainly by TKE, σ_w, and stability during turbulent conditions, while temperature dominates when weak-wind regime dominates. For CH_4, temperature is consistently important, with wind shear contributing under strong winds and advection (wind speed and direction) under weak winds. H_2O variability is strongly linked to temperature across all conditions, reflecting ET dynamics and energy gradients.

The analysis of FODS-derived potential temperature profiles

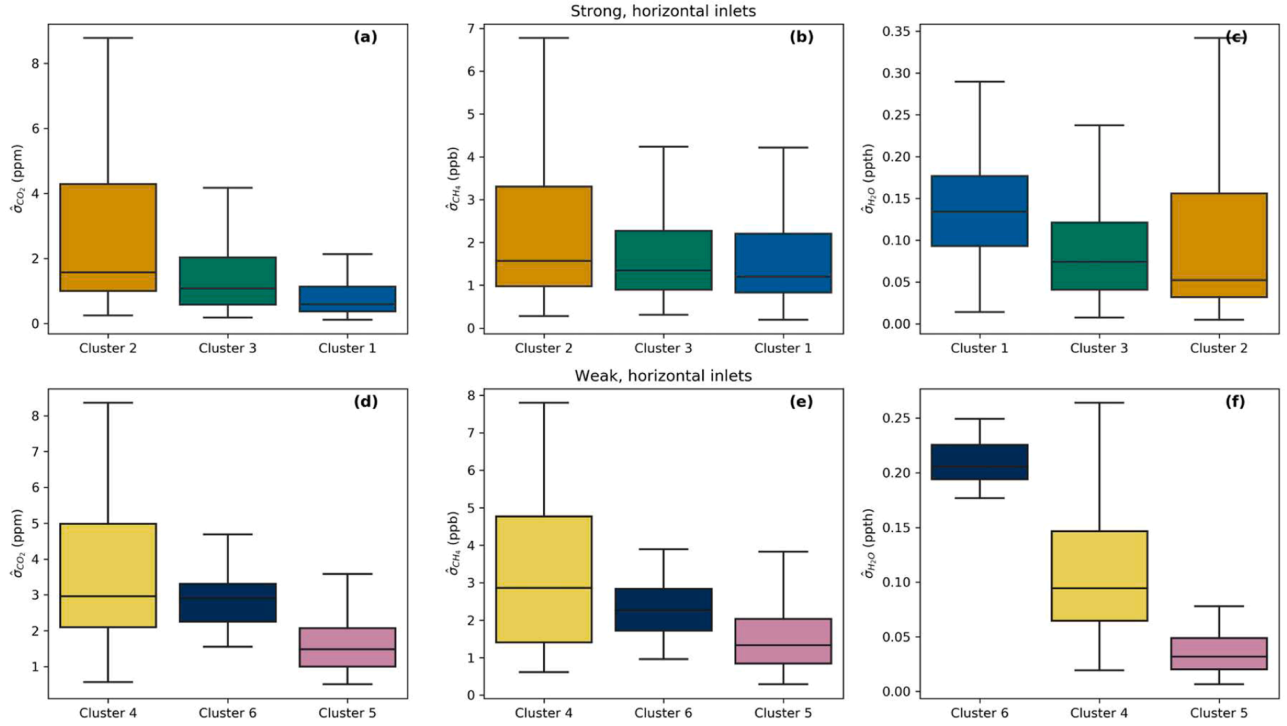

Fig. 11. Box plots of the horizontal spatial standard deviation of scalar gas concentrations ($\hat{\sigma}_{CO_2}$, $\hat{\sigma}_{CH_4}$, and $\hat{\sigma}_{H_2O}$) under strong-wind (a, b, c) and weak-wind (d, e, f) regimes. The regimes are defined based on the FODS potential temperature clusters at the main tower, as shown in Fig. 9a and b. Box plot colors correspond to the cluster colors used in Fig. 10. The horizontal line within each box represents the median, and the box plots are ordered by decreasing median values.

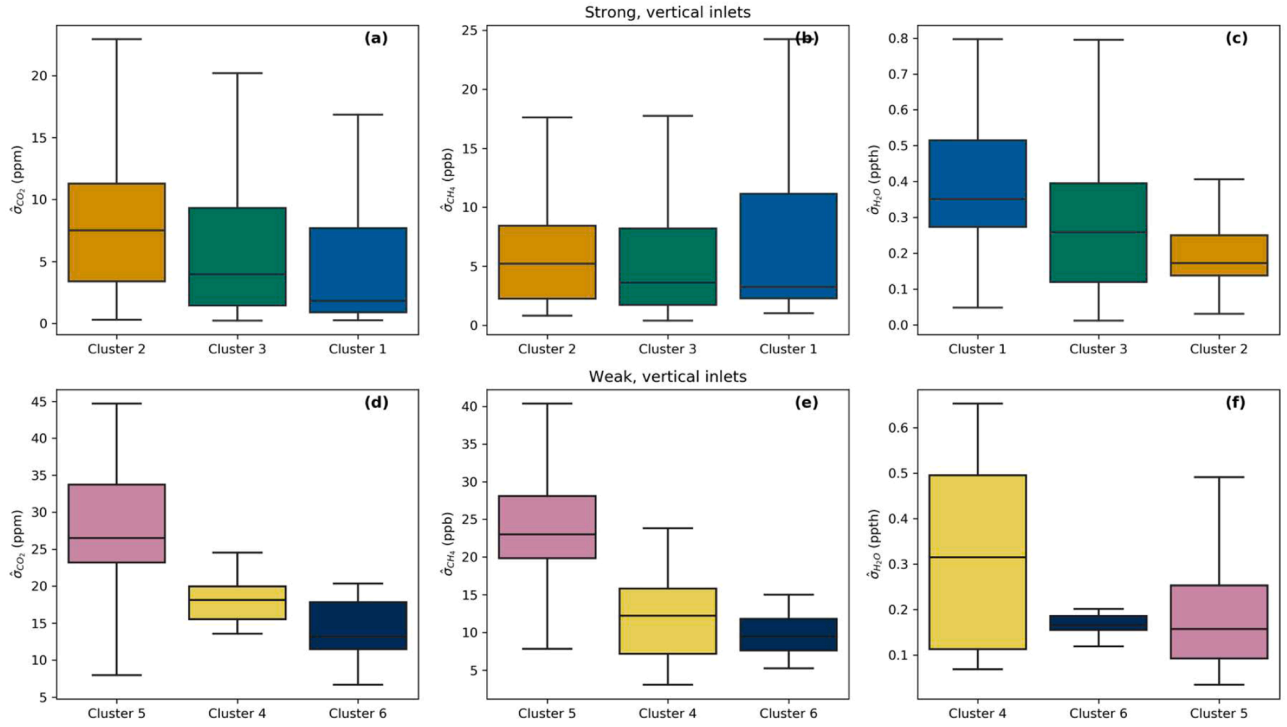

Fig. 12. Box plots of the vertical spatial standard deviation of scalar gas concentrations ($\hat{\sigma}_{CO_2}$, $\hat{\sigma}_{CH_4}$, and $\hat{\sigma}_{H_2O}$) under strong-wind (a, b, c) and weak-wind (d, e, f) regimes. The regimes are defined based on the FODS potential temperature clusters at the main tower, as shown in Fig. 10a and b. Box plot colors correspond to the cluster colors used in Fig. 10. The horizontal line within each box represents the median, and the box plots are ordered by decreasing median values.

highlights thermal stratification as a key driver of scalar gas variability, especially under weak-wind conditions. K-means clustering revealed distinct stratification regimes, with strong-wind periods marked by unstable profiles that enhance mixing, and weak-wind conditions dominated by stable layers that suppress turbulence, particularly near the forest floor and canopy top. This stratification strongly shapes the spatial variability of CO_2 and CH_4: unstable or near-neutral profiles enhance mixing and reduce variability, while stable conditions increase

scalar accumulation and spatial gradients. The potential temperature profile thus effectively integrates the influence of both turbulence and radiative processes on scalar dispersion. For horizontal variability, structural heterogeneity and differences in LAI further modulate gas transport by shaping local stratification and mixing conditions. However, water vapor variability follows a distinct pattern due to its ET-driven source, which is tightly linked to daytime energy input and plant physiological responses. Unlike CO_2 and CH_4, H_2O variability cannot be fully explained by thermal stratification alone; instead, it reflects a complex interaction of radiation, soil moisture, and canopy structure particularly during transition periods when residual ET persists under weakly stratified conditions.

These findings for drivers of scalar gas variability have practical implications beyond process-level understanding. By resolving fine-scale spatiotemporal patterns, our results can inform forest management strategies aimed at optimizing carbon sequestration and maintaining ecosystem health. They also provide valuable constraints for improving terrestrial greenhouse gas budgets and modeling trace gas exchange under different micrometeorological regimes, which is relevant for climate protection and mitigation efforts. Finally, the study demonstrates the utility of high-resolution sensor networks and combined observational–statistical approaches for capturing the complexity of forest-atmosphere interactions, which could benefit researchers and practitioners seeking to better quantify and predict ecosystem-scale gas fluxes.

CRediT authorship contribution statement

Mohammad Abdoli: Writing – review & editing, Writing – original draft, Visualization, Validation, Methodology, Investigation, Formal analysis, Data curation, Conceptualization. **Karl Lapo:** Writing – review & editing. **Christoph K. Thomas:** Writing – review & editing, Supervision, Resources, Project administration, Funding acquisition, Conceptualization.

Declaration of competing interest

In accordance with the journal's policy, I hereby declare that neither I nor my co-authors have any known competing financial interests or personal relationships that could have influenced the work presented in our manuscript entitled "Dynamic stability and canopy structure drive Spatio-Temporal Variability of Greenhouse Gas Concentrations in the Sub-canopy of a Temperate Spruce Forest."

We confirm that there are no conflicts of interest to disclose.

Acknowledgements

This research was supported by the European Research Council (ERC) under the Horizon 2020 programme (DarkMix, grant no. 724629). We gratefully acknowledge Elena Nitzler for her involvement in the scalar gas measurement campaign. We also thank Johann Schneider and Johannes Olesch for their valuable assistance with fieldwork and technical support.

Appendix A

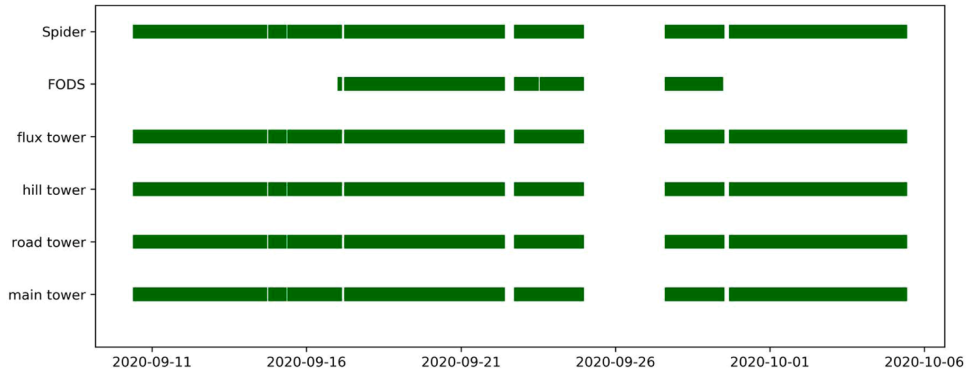

Fig. A1. Data availability of LOEWE20 experiment.

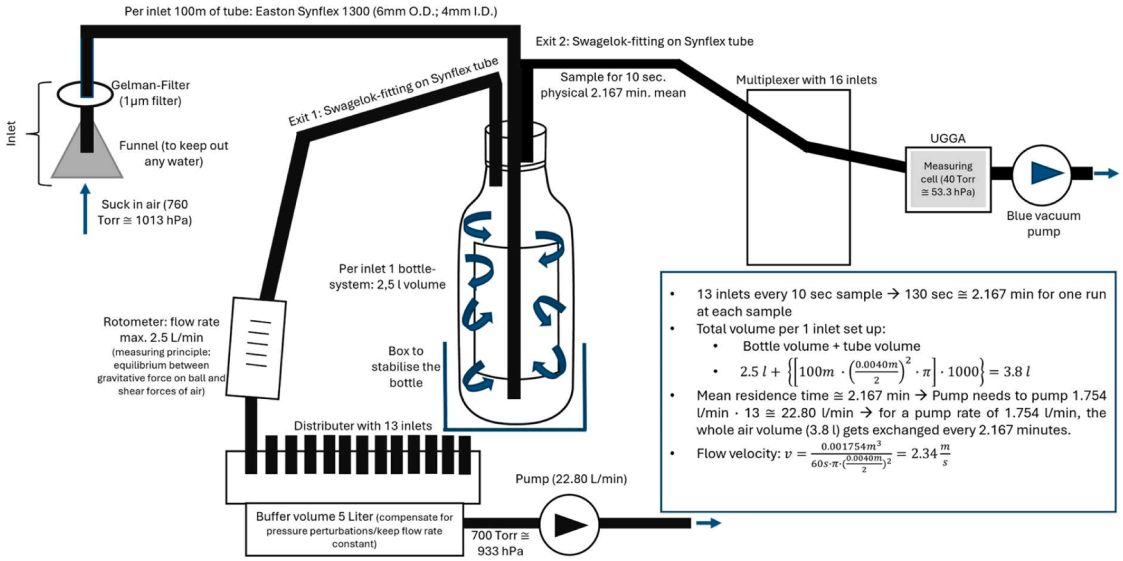

Fig. A2. Detailed design of the buffer and multiplexer system used in this study, including flow calculations (adapted from Nitzler, 2021).

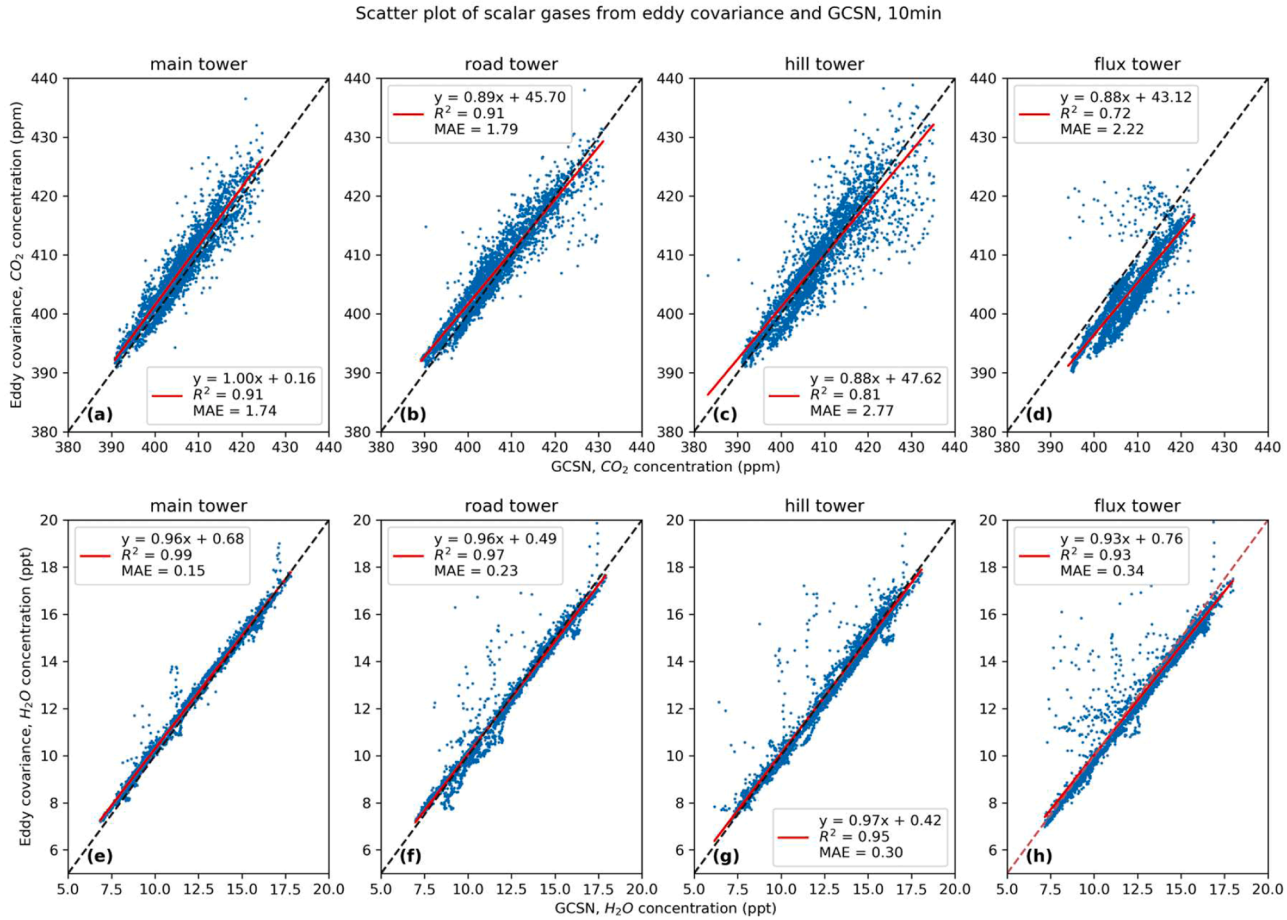

Fig. A3. Comparison between the scalar gas mixing ratio of close path gas analyser and EC. The inlet 7 was used for comparison with the EC tower at main tower EC (a, e), the inlet S8 used in road tower EC (b,f), the inlet 6 used for hill tower EC (c,g), and the inlet 9 used to be compared with flux tower EC.

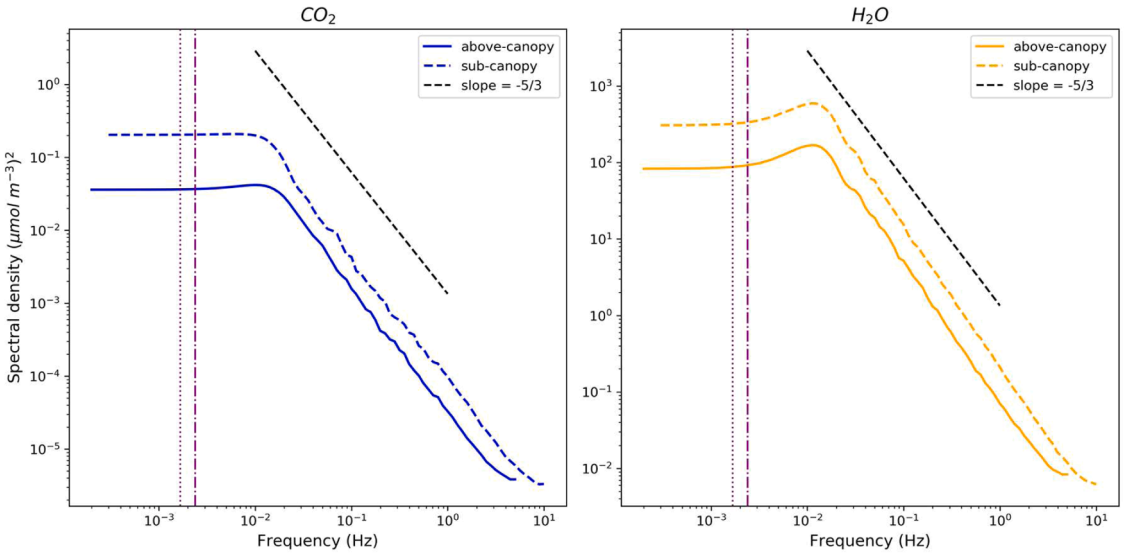

Fig. A4. Ensemble-averaged CO_2 and H_2O spectra are shown as a function of natural frequency (f) for both the above-canopy and sub-canopy measurements, for CO_2 on the left and H_2O on the right. One-minute averaged flux tower data was used for the above-canopy and road tower data was used for the sub-canopy. The ensemble averages were computed using 80 frequency bins. Vertical lines indicate averaging periods of 7 and 10 min, respectively.

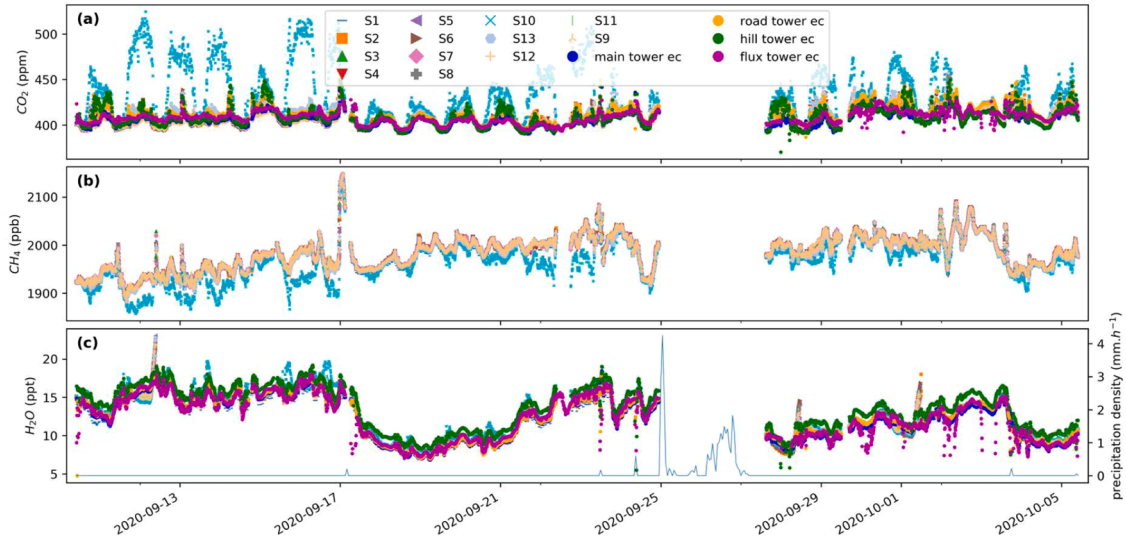

Fig. A5. (a) CO_2, (b) CH_4, and (c) H_2O mixing ratio and precipitation during LOEWE20 experiment. ppth stand for part per thousand, ppm for part per million, and ppb for part per billion.

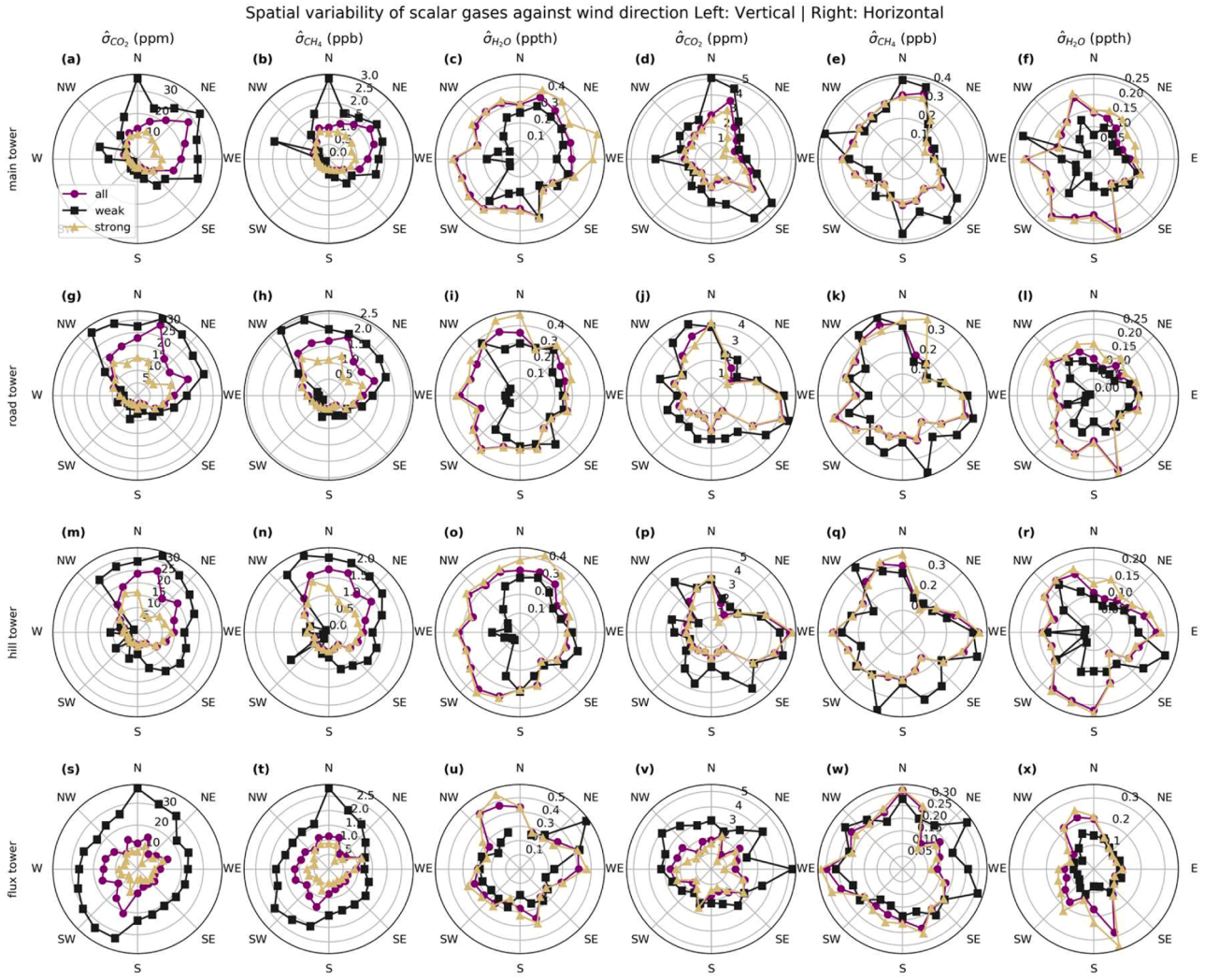

Fig. A6. Wind direction dependence of spatial variability in CO_2, CH_4, and H_2O mixing ratios in sub-canopy (first three rows), and above canopy (last row) in vertical (left) and horizontal (right) directions.

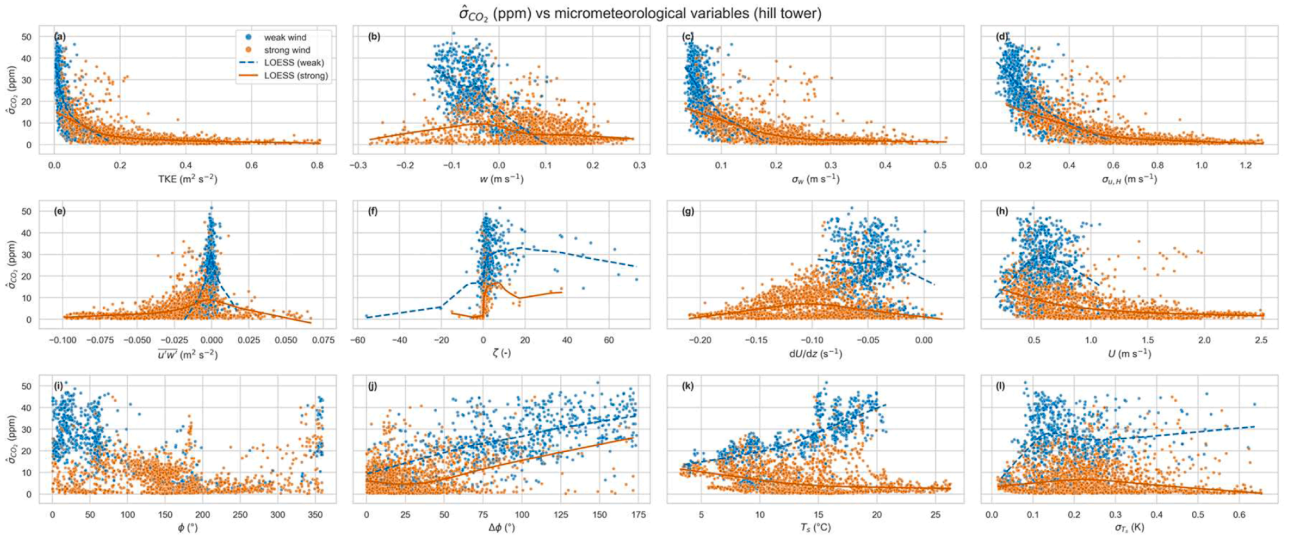

Fig. A7. Variation of micrometeorological variables with vertical $\widehat{\sigma}_{CO_2}$ at the hill tower under weak- and strong-wind regimes, with regime-specific Locally Estimated Scatterplot Smoothing (LOESS) fits.

Data availability

Data will be made available on request.

References

Abdoli, M., Lapo, K., Schneider, J., Olesch, J., Thomas, C.K., 2023. Toward quantifying turbulent vertical airflow and sensible heat flux in tall forest canopies using fiber-optic distributed temperature sensing. Atmospheric Meas. Tech. 16, 809–824. https://doi.org/10.5194/amt-16-809-2023.

Acevedo, O.C., Moraes, O.L., Degrazia, G.A., Fitzjarrald, D.R., Manzi, A.O., Campos, J.G., 2009. Is friction velocity the most appropriate scale for correcting nocturnal carbon dioxide fluxes? Agric. For. Meteorol. 149, 1–10.

Arcomano, T., Szunyogh, I., Pathak, J., Wikner, A., Hunt, B.R., Ott, E., 2020. A machine learning-based global atmospheric forecast model. Geophys. Res. Lett. 47, e2020GL087776.

Belcher, S., Finnigan, J., Harman, I., 2008. Flows through forest canopies in complex terrain. Ecol. Appl. 18, 1436–1453.

Bonan, G.B., 2008. Forests and climate change: forcings, feedbacks, and the climate benefits of forests. Science 320, 1444–1449.

Borken, W., Davidson, E.A., Savage, K., Sundquist, E.T., Steudler, P., 2006. Effect of summer throughfall exclusion, summer drought, and winter snow cover on methane fluxes in a temperate forest soil. Soil Biol. Biochem. 38, 1388–1395. https://doi.org/10.1016/j.soilbio.2005.10.011.

Botía, S., Gerbig, C., Marshall, J., Lavric, J.V., Walter, D., Pöhlker, C., Holanda, B., Fisch, G., de Araújo, A.C., Sá, M.O., Teixeira, P.R., Resende, A.F., Dias-Junior, C.Q., van Asperen, H., Oliveira, P.S., Stefanello, M., Acevedo, O.C., 2020. Understanding nighttime methane signals at the Amazon Tall Tower Observatory (ATTO). Atmospheric Chem. Phys. 20, 6583–6606. https://doi.org/10.5194/acp-20-6583-2020.

Breiman, L., 2001. Random forests. Mach. Learn. 45, 5–32.

des Tombe, B., Schilperoort, B., Bakker, M., 2020. Estimation of temperature and associated uncertainty from Fiber-optic raman-spectrum distributed temperature sensing. Sensors 20, 2235. https://doi.org/10.3390/s20082235.

Dupont, S., Irvine, M.R., Bonnefond, J.-M., Lamaud, E., Brunet, Y., 2012. Turbulent structures in a pine forest with a deep and sparse trunk space: stand and edge regions. Bound.-Layer Meteorol. 143, 309–336.

Dutaur, L., Verchot, L.V., 2007. A global inventory of the soil CH4 sink. Glob. Biogeochem. Cycles 21. https://doi.org/10.1029/2006GB002734.

Feigenwinter, C., Mölder, M., Lindroth, A., Aubinet, M., 2010. Spatiotemporal evolution of CO2 concentration, temperature, and wind field during stable nights at the Norunda forest site. Agric. For. Meteorol. 150, 692–701.

Feng, H., Guo, J., Han, M., Wang, W., Peng, C., Jin, J., Song, X., Yu, S., 2020. A review of the mechanisms and controlling factors of methane dynamics in forest ecosystems. For. Ecol. Manag. 455, 117702.

Foken, T., 2017. Energy and Matter Fluxes of a Spruce Forest Ecosystem. Springer.

Freundorfer, A., Lapo, K., Schneider, J., Thomas, C.K., 2021. Distributed sensing of wind direction using Fiber-optic cables. J. Atmospheric Ocean. Technol. 38, 1871–1883. https://doi.org/10.1175/JTECH-D-21-0019.1.

Freundorfer, A., Rehberg, I., Law, B.E., Thomas, C., 2019. Forest wind regimes and their implications on cross-canopy coupling. Agric. For. Meteorol. 279, 107696.

Girach, I.A., Ponmalar, M., Murugan, S., Rahman, P.A., Babu, S.S., Ramachandran, R., 2022. Applicability of machine learning model to simulate atmospheric CO_2 variability. IEEE Trans. Geosci. Remote Sens. 60, 1–6.

Harazono, Y., Iwata, H., Sakabe, A., Ueyama, M., Takahashi, K., Nagano, H., Nakai, T., Kosugi, Y., 2015. Effects of water vapor dilution on trace gas flux, and practical correction methods. J. Agric. Meteorol. 71, 65–76. https://doi.org/10.2480/agrmet.D-14-00003.

Jain, A.K., 2010. Data clustering: 50 years beyond K-means. Pattern Recognit. Lett. 31, 651–666.

Kanani-Sühring, F., Raasch, S., 2015. Spatial variability of scalar concentrations and fluxes downstream of a clearing-to-forest transition: a large-eddy simulation study. Bound.-Layer Meteorol 155, 1–27.

Krebs, L., Burri, S., Feigenwinter, I., Gharun, M., Meier, P., Buchmann, N., 2024. Forest-floor respiration, N_2O fluxes, and CH_4 fluxes in a subalpine spruce forest: drivers and annual budgets. Biogeosciences 21, 2005–2028. https://doi.org/10.5194/bg-21-2005-2024.

Lapo, K., Freundorfer, A., 2020. Klapo/Pyfocs v0. 5. Zenodo Genève Switz.

Lapo, K., Freundorfer, A., Pfister, L., Schneider, J., Selker, J., Thomas, C., 2020. Distributed observations of wind direction using microstructures attached to actively heated fiber-optic cables. Atmospheric Meas. Tech. 13, 1563–1573. https://doi.org/10.5194/amt-13-1563-2020.

Liang, J., Zhang, L., Wang, Y., Cao, X., Zhang, Q., Wang, H., Zhang, B., 2014. Turbulence regimes and the validity of similarity theory in the stable boundary layer over complex terrain of the Loess Plateau, China. J. Geophys. Res. Atmospheres 119, 6009–6021. https://doi.org/10.1002/2014JD021510.

Mahrt, L., Sun, J., Stauffer, D., 2015. Dependence of turbulent velocities on wind speed and stratification. Bound.-Layer Meteorol. 155, 55–71. https://doi.org/10.1007/s10546-014-9992-5.

Ni, X., Groffman, P.M., 2018. Declines in methane uptake in forest soils. Proc. Natl. Acad. Sci 115, 8587–8590. https://doi.org/10.1073/pnas.1807377115.

Nitzler, E., 2021. An experimental analysis of pressure pumping at the air-soil interface in a moderately dense spruce forest, Waldstein, Germany.

Oliveira, P.E., Acevedo, O.C., Sörgel, M., Tsokankunku, A., Wolff, S., Araújo, A.C., Souza, R.A., Sá, M.O., Manzi, A.O., Andreae, M.O., 2018. Nighttime wind and scalar variability within and above an Amazonian canopy. Atmospheric Chem. Phys. 18, 3083–3099.

Pedregosa, F., Varoquaux, G., Gramfort, A., Michel, V., Thirion, B., Grisel, O., Blondel, M., Prettenhofer, P., Weiss, R., Dubourg, V., 2011. Scikit-learn: machine learning in Python. J. Mach. Learn. Res. 12, 2825–2830.

Pettitt, A.N., 1979. A non-parametric approach to the change-point problem. J. R. Stat. Soc. Ser. C Appl. Stat. 28, 126–135.

Querino, C.a.S., Smeets, C.J.P.P., Vigano, I., Holzinger, R., Moura, V., Gatti, L.V., Martinewski, A., Manzi, A.O., de Araújo, A.C., Röckmann, T., 2011. Methane flux, vertical gradient and mixing ratio measurements in a tropical forest. Atmospheric Chem. Phys. 11, 7943–7953. https://doi.org/10.5194/acp-11-7943-2011.

Raupach, M.R., 1989. Applying lagrangian fluid mechanics to infer scalar source distributions from concentration profiles in plant canopies. Agric. For. Meteorol. Biometeorol. 47, 85–108. https://doi.org/10.1016/0168-1923(89)90089-0.

Raupach, M.R., Finnigan, J.J., Brunet, Y., 1996. Coherent eddies and turbulence in vegetation canopies: the mixing-layer analogy. In: Garratt, J.R., Taylor, P.A. (Eds.), Boundary-Layer Meteorology 25th Anniversary Volume, 1970–1995: Invited Reviews and Selected Contributions to Recognise Ted Munn's Contribution As Editor over the Past 25 Years. Springer, Netherlands, Dordrecht, pp. 351–382. https://doi.org/10.1007/978-94-017-0944-6_15.

Rodrigues, A., Sardinha, R.A., Pita, G., 2021. Aerodynamic characterization of the surface layer. In: Rodrigues, A., Sardinha, R.A., Pita, G. (Eds.), Fundamental Principles of Environmental Physics. Springer International Publishing, Cham, pp. 13–32. https://doi.org/10.1007/978-3-030-69025-0_2.

Ruehr, N.K., Knohl, A., Buchmann, N., 2010. Environmental variables controlling soil respiration on diurnal, seasonal and annual time-scales in a mixed mountain forest in Switzerland. Biogeochemistry 98, 153–170. https://doi.org/10.1007/s10533-009-9383-z.

Sayde, C., Thomas, C.K., Wagner, J., Selker, J., 2015. High-resolution wind speed measurements using actively heated fiber optics. Geophys. Res. Lett. 42, 10064–10073. https://doi.org/10.1002/2015GL066729.

Schilperoort, B., Coenders-Gerrits, M., Jiménez Rodríguez, C., van der Tol, C., Van De Wiel, B., Savenije, H., 2020. Decoupling of a Douglas fir canopy: a look into the subcanopy with continuous vertical temperature profiles. Biogeosciences Discuss 2020, 1–25.

Serafimovich, A., Thomas, C., Foken, T., 2011. Vertical and horizontal transport of energy and matter by coherent motions in a tall spruce canopy. Bound.-Layer Meteorol. 140, 429–451.

Shen, Q., Gao, G., Fu, B., Lü, Y., 2015. Responses of shelterbelt stand transpiration to drought and groundwater variations in an arid inland river basin of Northwest China. J. Hydrol. 531, 738–748. https://doi.org/10.1016/j.jhydrol.2015.10.053.

Song, J., Gkatzelis, G.I., Tillmann, R., Brüggemann, N., Leisner, T., Saathoff, H., 2024. Characterization of biogenic volatile organic compounds and their oxidation products in a stressed spruce-dominated forest close to a biogas power plant. Atmospheric Chem. Phys. 24, 13199–13217. https://doi.org/10.5194/acp-24-13199-2024.

Stiegler, C., June, T., Markwitz, C., Camarretta, N., Ali, A.A., Knohl, A., 2023. Wind regimes above and below a dense oil palm canopy: detection of decoupling and its implications on CO2 flux estimates. Agric. For. Meteorol. 341, 109668. https://doi.org/10.1016/j.agrformet.2023.109668.

Sun, J., Mahrt, L., Banta, R.M., Pichugina, Y.L., 2012. Turbulence regimes and turbulence intermittency in the stable boundary layer during CASES-99. J Atmos Sci 69, 338–351.

Sundqvist, E., Mölder, M., Crill, P., Kljun, N., Lindroth, A., 2015. Methane exchange in a boreal forest estimated by gradient method. Tellus B Chem. Phys. Meteorol. 67. https://doi.org/10.3402/tellusb.v67.26688.

Thomas, C., Foken, T., 2007a. Organised motion in a tall spruce canopy: temporal scales, structure spacing and terrain effects. Bound.-Layer Meteorol. 122, 123–147. https://doi.org/10.1007/s10546-006-9087-z.

Thomas, C., Foken, T., 2007b. Flux contribution of coherent structures and its implications for the exchange of energy and matter in a tall spruce canopy. Bound.-Layer Meteorol 123, 317–337.

Thomas, C.K., 2011. Variability of sub-canopy flow, temperature, and horizontal advection in moderately complex terrain. Bound.-Layer Meteorol 139, 61–81.

Thomas, C.K., Huss, J.-M., Abdoli, M., Huttarsch, T., Schneider, J., 2022. Solid-phase reference baths for Fiber-optic distributed sensing. Sensors 22, 4244.

Thomas, C.K., Law, B.E., Irvine, J., Martin, J.G., Pettijohn, J.C., Davis, K.J., 2009. Seasonal hydrology explains interannual and seasonal variation in carbon and water exchange in a semiarid mature ponderosa pine forest in central Oregon. J. Geophys. Res. Biogeosciences 114.

Thomas, C.K., Martin, J.G., Law, B.E., Davis, K., 2013. Toward biologically meaningful net carbon exchange estimates for tall, dense canopies: multi-level eddy covariance observations and canopy coupling regimes in a mature Douglas-fir forest in Oregon. Agric. For. Meteorol. 173, 14–27.

Thomas, C.K., Selker, J., 2021. Optical Fiber-based distributed sensing methods. In: Foken, T. (Ed.), Springer Handbook of Atmospheric Measurements. Springer International Publishing, Cham, pp. 609–631. https://doi.org/10.1007/978-3-030-52171-4_20.

Van de Giesen, N., Steele-Dunne, S.C., Jansen, J., Hoes, O., Hausner, M.B., Tyler, S., Selker, J., 2012. Double-ended calibration of fiber-optic Raman spectra distributed temperature sensing data. Sensors 12, 5471–5485.

van Ramshorst, J.G.V., Coenders-Gerrits, M., Schilperoort, B., van de Wiel, B.J.H., Izett, J.G., Selker, J.S., Higgins, C.W., Savenije, H.H.G., van de Giesen, N.C., 2020. Revisiting wind speed measurements using actively heated fiber optics: a wind

tunnel study. Atmospheric Meas. Tech. 13, 5423–5439. https://doi.org/10.5194/amt-13-5423-2020.
Vickers, D., Thomas, C.K., 2014. Observations of the scale-dependent turbulence and evaluation of the flux–gradient relationship for sensible heat for a closed Douglas-fir canopy in very weak wind conditions. Atmos. Chem. Phys. 14, 9665–9676.
Wilson, K.B., Meyers, T.P., 2001. The spatial variability of energy and carbon dioxide fluxes at the floor of a deciduous forest. Bound.-Layer Meteorol. 98, 443–473.